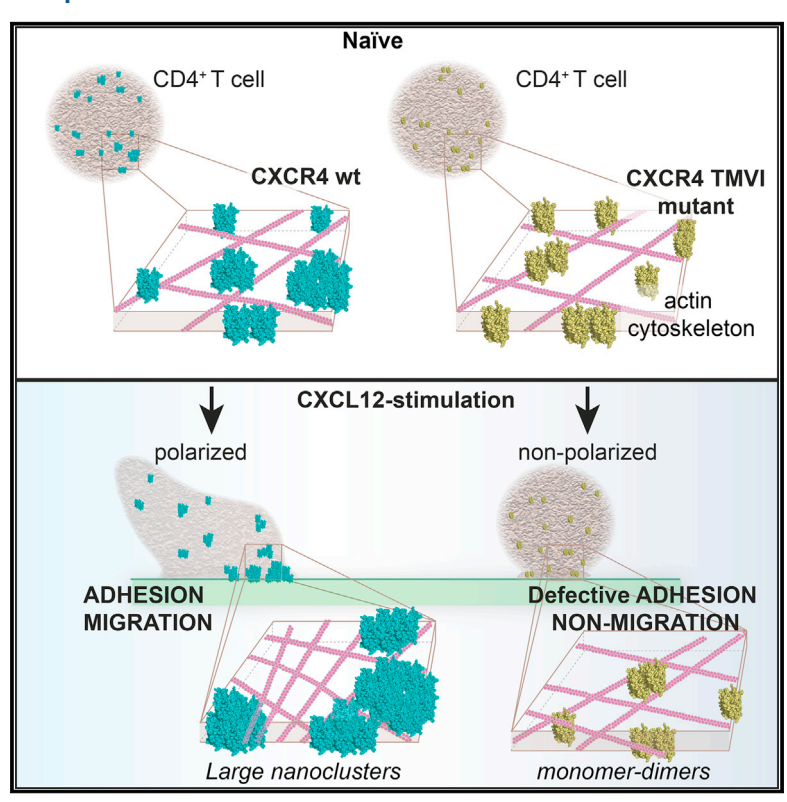
# **Molecular Cell**

# Separating Actin-Dependent Chemokine Receptor Nanoclustering from Dimerization Indicates a Role for Clustering in CXCR4 Signaling and Function

# **Graphical Abstract**



# **Highlights**

- CXCR4 is organized at the T cell membrane as monomers, dimers, and basal nanoclusters
- The actin cytoskeleton and CD4 regulate CXCL12 induction of large CXCR4 nanoclusters
- CXCR4 TMVI structural motifs also govern its spatiotemporal organization
- CXCR4 nanocluster size defines its dynamics and its ability to trigger cell function

# **Authors**

Laura Martínez-Muñoz, José Miguel Rodríguez-Frade, Rubén Barroso, ..., Francisco Sánchez-Madrid, María F. García-Parajo, Mario Mellado

# Correspondence

laura.martinez@cabimer.es (L.M.-M.), mmellado@cnb.csic.es (M.M.)

## In Brief

Martínez-Muñoz and colleagues show that CXCR4 forms monomers, dimers, and nanoclusters at the T cell membrane. Their nanoscale organization is governed by local organizers such as CD4 and the actin cytoskeleton, and by structural motifs in the CXCR4 TMVI region. CXCL12 promotes larger CXCR4 nanoclusters needed for complete cell function.







# Separating Actin-Dependent Chemokine Receptor Nanoclustering from Dimerization Indicates a Role for Clustering in CXCR4 Signaling and Function

Laura Martínez-Muñoz, 1,2,\* José Miguel Rodríguez-Frade, 1 Rubén Barroso, 1 Carlos Óscar S. Sorzano, 3 Juan A. Torreño-Pina,<sup>4</sup> César A. Santiago,<sup>5</sup> Carlo Manzo,<sup>4,6</sup> Pilar Lucas,<sup>1</sup> Eva M. García-Cuesta,<sup>1</sup> Enric Gutierrez,<sup>4</sup> Laura Barrio, <sup>7</sup> Javier Vargas, <sup>3,8</sup> Graciela Cascio, <sup>1</sup> Yolanda R. Carrasco, <sup>7</sup> Francisco Sánchez-Madrid, <sup>9</sup> María F. García-Parajo, 4,10 and Mario Mellado 1,11,\*

# **SUMMARY**

A current challenge in cell motility studies is to understand the molecular and physical mechanisms that govern chemokine receptor nanoscale organization at the cell membrane, and their influence on cell response. Using single-particle tracking and superresolution microscopy, we found that the chemokine receptor CXCR4 forms basal nanoclusters in resting T cells, whose extent, dynamics, and signaling strength are modulated by the orchestrated action of the actin cytoskeleton, the co-receptor CD4, and its ligand CXCL12. We identified three CXCR4 structural residues that are crucial for nanoclustering and generated an oligomerization-defective mutant that dimerized but did not form nanoclusters in response to CXCL12, which severely impaired signaling. Overall, our data provide new insights to the field of chemokine biology by showing that receptor dimerization in the absence of nanoclustering is unable to fully support CXCL12-mediated responses, including signaling and cell function in vivo.

#### INTRODUCTION

Cell migration is a coordinated process that requires rapid integration of extracellular stimuli and intracellular signaling. Cells migrate toward chemoattractant gradients, which activate the cells by binding receptors of the GPCR (G-protein-coupled receptor) family. Although many studies have defined the role of these receptors in chemokine function (Griffith et al., 2014) and analyzed the signaling cascades involved in detail (Thelen, 2001), little is known of their spatiotemporal organization at the cell surface, the factors that participate in their control, or their influence on chemokine biology.

Receptor nanoclustering and dynamics are needed to transduce signals and respond to extracellular stimuli. The GPCR exist as monomers, dimers, and higher-order oligomers, all of which assemble into homo- and hetero-oligomeric structures (Palczewski, 2010). These nanoclusters are in dynamic equilibrium, with constant aggregation and dissociation to generate new receptor complexes (Calebiro et al., 2013). Many factors are involved in the regulation of GPCR nanoclustering (Calebiro et al., 2013; Hauser et al., 2016), including transmembrane proteins (Bethani et al., 2010), cell membrane lipid composition (Marino et al., 2016), and the actin cytoskeleton (Scarselli et al., 2012), which regulates trafficking of signaling molecules and partitions the membrane into microdomains (Kusumi et al., 2005). Nanoclustering and dynamics are especially relevant for chemokine receptors, as they allow the cell to correctly sense gradients and move appropriately. Chemokines also regulate actin cytoskeleton dynamics (Vicente-Manzanares and Sánchez-Madrid, 2004), coordinating cell responses (Brzostowski et al., 2013).

The chemokine receptor CXCR4 and its ligand CXCL12 form a key pair in development, hematopoiesis, neutrophil homeostasis, and lymphocyte trafficking (Eash et al., 2010; Zou et al., 1998). Mice that lack CXCR4 die perinatally due to developmental, hematopoietic, and cardiogenetic defects (Ma et al.,



<sup>&</sup>lt;sup>1</sup>Chemokine Signaling Group, Department of Immunology and Oncology, Centro Nacional de Biotecnología (CNB-CSIC), Campus de Cantoblanco, 28049 Madrid, Spain

<sup>&</sup>lt;sup>2</sup>Department of Cell Signaling, Centro Andaluz de Biología Molecular y Medicina Regenerativa (CSIC), 41092 Sevilla, Spain

<sup>&</sup>lt;sup>3</sup>Biocomputing Unit, Centro Nacional de Biotecnología (CNB-CSIC), Campus de Cantoblanco, 28049 Madrid, Spain

<sup>&</sup>lt;sup>4</sup>ICFO-Institut de Ciencies Fotoniques, The Barcelona Institute of Science and Technology, 08860 Barcelona, Spain

<sup>&</sup>lt;sup>5</sup>X-ray Crystallography Unit, Centro Nacional de Biotecnología (CNB-CSIC), Campus de Cantoblanco, 28049 Madrid, Spain <sup>6</sup>Universitat de Vic, Universitat Central de Catalunya (UVic-UCC), 08500 Vic, Spain

<sup>&</sup>lt;sup>7</sup>B Cell Dynamics Group, Department of Immunology and Oncology, Centro Nacional de Biotecnología (CNB-CSIC), Campus de Cantoblanco, 28049 Madrid, Spain

<sup>&</sup>lt;sup>8</sup>Department of Anatomy and Cell Biology, McGill University, Montreal, QC, Canada

<sup>&</sup>lt;sup>9</sup>Laboratory of Intercellular Communication, Fundación CNIC, Madrid 28029, Spain

<sup>&</sup>lt;sup>10</sup>ICREA, Pg. Lluís Companys 23, 08010 Barcelona, Spain

<sup>&</sup>lt;sup>11</sup>Lead Contact

<sup>\*</sup>Correspondence: laura.martinez@cabimer.es (L.M.-M.), mmellado@cnb.csic.es (M.M.) https://doi.org/10.1016/j.molcel.2018.02.034

1998; Tachibana et al., 1998). In humans, the CXCR4/CXCL12 axis is involved in tumor progression and metastasis (Teicher and Fricker, 2010), pulmonary fibrosis (Xu et al., 2007), HIV-1 infection (Bleul et al., 1996), and autoimmune disease (Hansen et al., 2006).

As for other chemokine receptors, CXCR4 form homo- and heterodimers (Muñoz et al., 2011), as well as trimeric complexes (Hamatake et al., 2009). In the presence of antagonists, the crystal structure of CXCR4 showed a homodimeric conformation whose interface is located in transmembrane regions (Wu et al., 2010). The CXCL12-triggered pathways have been studied, but the molecular and physical mechanisms that control CXCR4 organization at the cell membrane and how the cell integrates further signals and responses are largely unknown.

Here, we used quantitative single-molecule spatiodynamic imaging and super-resolution microscopy to elucidate the molecular organization, membrane partners, structural motifs, and signaling of resting and activated CXCR4 in human T cells. Our results indicate that, in addition to the ligand-mediated conformational change of the receptor that activates G protein, changes associated with receptor nanoclustering are necessary for full function. We identified an essential role for lateral partitioning of these receptors into nanoclusters in the regulation of chemokine-mediated signaling and establish a new target for potential intervention in chemokine functions.

# **RESULTS**

# CXCR4 Forms Basal Nanoclusters with Distinct Types of Mobilities on T Cells

Class A GPCR form oligomers at the cell surface (Calebiro et al., 2013); these complexes define the signaling pathway activated through ligand binding (Hauser et al., 2016). We used stimulated emission depletion (STED) super-resolution microscopy to visualize CXCR4 nanoscale organization in primary naive CD4 $^{\rm +}$  T lymphocyte cells (T cells) and in the Jurkat CD4 $^{\rm +}$  T cell line. With a STED spatial resolution of  ${\sim}60$  nm, we distinguished individual CXCR4-fluorescent spots (Figures 1A and 1B), which we analyzed in terms of intensity and receptor number. Receptors co-existed as monomers and dimers ( ${\sim}80\%$  in T cells and  ${\sim}35\%$  in Jurkat CD4 $^{\rm +}$  cells) but also formed nanoclusters of more than three receptors ( ${\sim}20\%$  and 65%, respectively) (Figures 1A and 1B).

To assess CXCR4 dynamics, we used single-particle tracking (SPT) in total internal reflection fluorescence (TIRF) mode and transfected Jurkat CD4<sup>+</sup> cells with CXCR4 fused to the AcGFP monomeric protein (JKCD4). We first determined appropriate expression conditions for detecting and tracking individual CXCR4 spots. Only movies with densities ≤4.5 particles/μm² (~8,500–22,000 receptors/cell) were used to detect and track CXCR4. Receptor trajectories were reconstructed using a tracking algorithm to follow individual particles (Jaqaman et al., 2008) (Figure 1C; Movies S1 and S2). In steady state, ~28% of CXCR4 particles were classified as immobile (Figures 1D and S1A). The remaining mobile receptors showed distinct diffusion profiles derived from mean square displacement (MSD) plots (Figures 1E), (Manzo and Garcia-Parajo, 2015) and were further

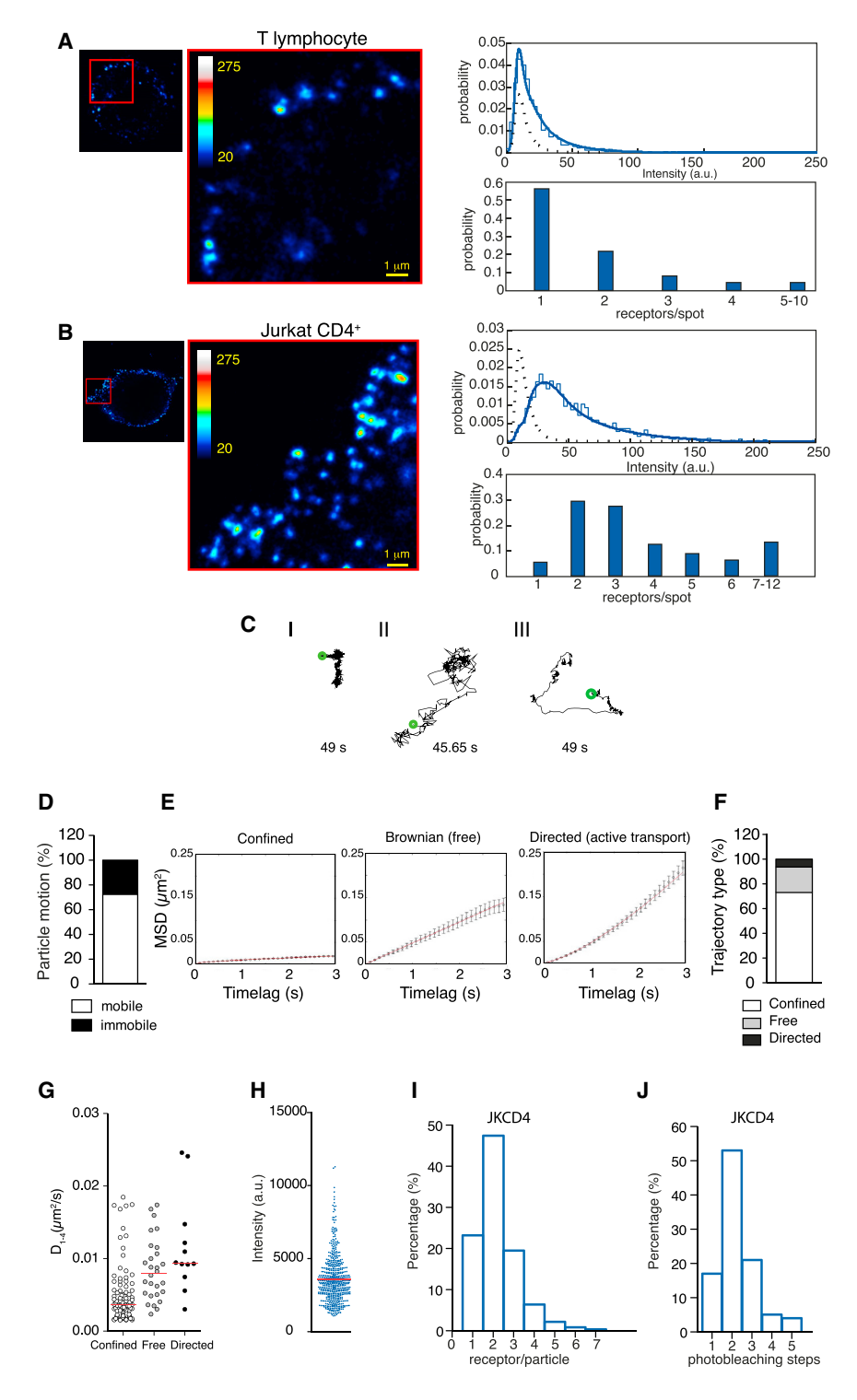
classified based on motion, using the moment scaling spectrum (MSS) (Ewers et al., 2005). For most mobile particles (~78%), diffusion was confined within ~200-nm regions (Figures S1B and S1C);  $\sim$ 15% showed Brownian-free diffusion and  $\sim$ 7% exhibited directed motion (Figure 1F). The median value of the short time-lag diffusion coefficient (D<sub>1-4</sub>) for CXCR4 trajectories varied from 0.0037  $\mu m^2 s^{-1}$  for confined receptors to 0.0094  $\mu m^2 s^{-1}$  for CXCR4 with direct-transport motion (Figure 1G). To determine receptor number in individual trajectories, we measured the average fluorescence intensity for the first 20 frames of each trajectory (Figure 1H) and used intensity of the monomeric protein CD86-AcGFP as reference (Calebiro et al., 2013) (Figures S1D-S1F). We found CXCR4 monomers (~23%) and dimers  $(\sim 47\%)$ , as well as complexes with more than three receptors (~30%) (Figure 1I). Alternative evaluation of TIRF trajectories using single-step photobleaching analysis confirmed these data (Figures 1J and S1G).

Results for JKCD4 cells compared with those for Jurkat CD4<sup>+</sup> cells in which endogenous CXCR4 was small interfering RNA (siRNA) downregulated before CXCR4-AcGFP transfection (JK<sup>-</sup>CD4) showed a minimal effect of endogenous CXCR4 on particle distribution (Figures S2A–S2C). The data indicate that endogenous CXCR4 does not affect our main observation that dynamic CXCR4 monomers, dimers, and small nanoclusters coexist at the steady-state T cell membrane.

# CXCL12 Binding Modulates CXCR4 Dynamics and Enhances Nanoclustering

As CXCL12 binding to the receptor promotes conformational changes in CXCR4 and increases CXCR4 dimer numbers (Schiraldi et al., 2012), we used SPT to evaluate the effect of saturating ligand concentrations on CXCR4 dynamics. JKCD4 cells were plated on fibronectin- or fibronectin/CXCL12-coated plates, and the lateral mobility of individual particles was followed over time. CXCL12 promoted a significant reduction in overall CXCR4 diffusivity (basal, median  $D_{1-4} = 0.0047 \mu m^2 s^{-1}$ ; CXCL12, median  $D_{1-4} = 0.0042 \mu m^2 s^{-1}$ ) and increased the percentage of immobile particles from  $\sim\!27\%$  (basal) to  $\sim\!35\%$ (CXCL12) (Figures 2A and 2B; Movies S3 and S4). These data agree with those reported for another agonist-activated GPCR (Baker et al., 2007). We also detected an increase in larger nanoclusters at the membrane of CXCL12-activated cells (~70% of nanoclusters with  $\geq 3$  receptors, compared to  $\sim 30\%$  of similar nanoclusters in basal conditions (Figure 2C); ~22% of immobile particles were nanoclusters formed by ≥3 receptors/particle compared to  $\sim$ 7% in steady state (Figure 2D). When only larger nanoclusters (4-7 receptors/particle) were considered, differences were even greater.

Some reports associate receptor oligomerization to signaling (Jaqaman and Grinstein, 2012) and show that cluster size influences receptor dynamics (Calebiro et al., 2013; Jaqaman et al., 2011). When compared to steady-state conditions, CXCL12-stimulated cells showed no changes in the relative percentage of trajectories showing different types of diffusion (Figure 2E). The fraction containing monomers and dimers with confined and Brownian motions generally diffused more slowly after CXCL12 binding, as did confined nanoclusters (although the last was not statistically significant) (Figure 2F). Results



were similar for JK-CD4 cells (Figure S2D). To confirm increased CXCR4 nanoclustering after CXCL12 stimulation, we performed STED imaging on Jurkat CD4+ cells and T cells; CXCL12 promoted CXCR4 nanoclustering to a maximum of 10-18 receptors/particle (Figures 2G and 2H). The ligand thus reduced the percentage of monomers and dimers at the expense of

Figure 1. CXCR4 Forms Nanoclusters and Shows Various Types of Motion at the T Cell Surface

(A and B) Representative STED images of CXCR4 on steady-state cells, T cells (A), and Jurkat CD4+ cells (B), with zooms of specific membrane regions (insets). The pseudo-color-code scale denotes the intensity of individual CXCR4/AF488-labeled spots, from dimer (dark blue) to nanocluster (redto-white). Bar, 1 µm. Intensity distribution (top plot) of individual CXCR4 spots on the cell membrane (solid line) and of single antibodies attached nonspecifically to glass (dashed line), from STED images, is shown. Probability histograms (bottom plot) of CXCR4 receptor distribution, retrieved from analysis of the intensity distribution data, are shown. Spots for Jurkat CD4+ cells (2076) and T cells (2575) from 30 cells in independent STED experiments (n = 2-3) are shown.

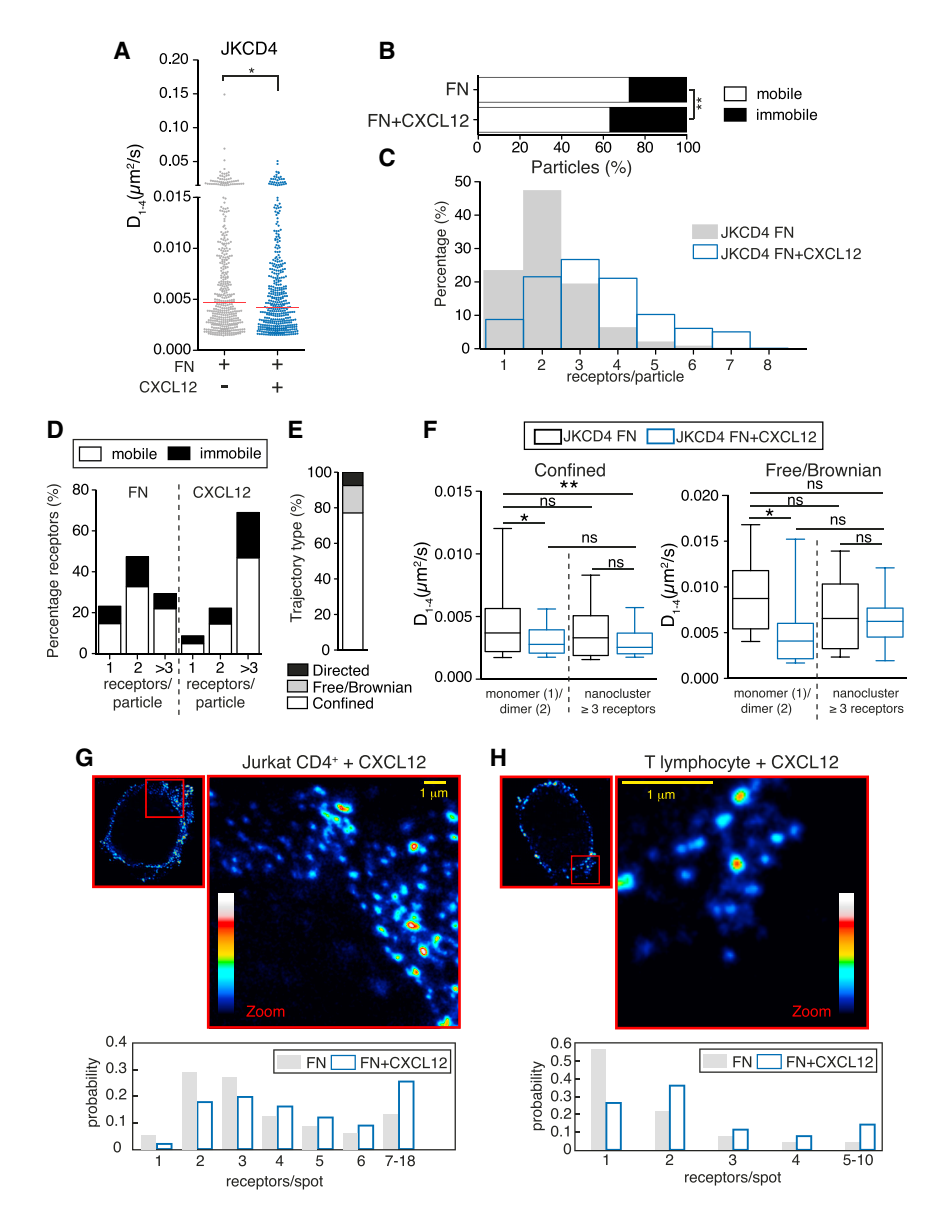
- (C) Representative trajectories (I, confined, II, Brownian/free, III, direct transport) of CXCR4-AcGFP particles diffusing at the membrane at indicated times, detected by SPT-TIRF in resting JKCD4 cells. The centroid position of the spot (green circle) was tracked (black line).
- (D) Percentage of CXCR4-AcGFP trajectories classified as immobile or mobile (593 trajectories from 22 JKCD4 cells, n = 3).
- (E) Representative MSD plots from individual trajectories of CXCR4-AcGFP showing different types of motion.
- (F) Percentage of single trajectories with different types of motion, classified by MSS (192 trajectories from 22 cells, n = 3).
- (G) Short time-lag diffusion coefficients ( $D_{1-4}$ ) from individual trajectories analyzed in (F), with median (red).
- (H) Intensity distribution from individual CXCR4-AcGFP trajectories, averaged over the first 20 frames and background subtracted (595 trajectories, n = 5), mean (red).
- (I) Percentage of receptor/particle number as extracted from the intensity distribution of individual CXCR4-AcGFP trajectories (H) (see STAR Methods).
- (J) Percentage of discrete photobleaching steps from individual CXCR4-AcGFP trajectories (151 trajectories from 8 cells, n = 2).

See also Figures S1 and S2 and Movies S1 and S2.

increasing the number of large nanoclusters and promoting their immobilization.

Agonist-mediated internalization is associated with clathrin-mediated endocytosis of chemokine receptors (Venkatesan et al., 2003). We found that CXCL12-

mediated nanoclusters remained unaltered after cell treatment with PitStop2 or brefeldin A, drugs that block clathrin vesicle formation and intracellular protein transport, respectively (Figures S2E and S2F). These data strongly suggest that these nanoclusters correspond to membrane-bound receptors, which is consistent with the low percentage of trajectories



showing directed motion (an indication of vesicular transport) (Figure 2E).

# **CD4 Co-expression Alters CXCR4 Homodimerization, Clustering, and Diffusion Dynamics**

CXCR4 diffusion at the cell membrane might be influenced by external factors such as the membrane-skeleton or by other transmembrane proteins, as suggested for other receptors (Kusumi et al., 2005). CXCR4 interaction with CD4 is essential for HIV-1 infection (Martínez-Muñoz et al., 2014). We assessed the presence of CD4/CXCR4 complexes by fluorescence resonance energy transfer (FRET) (Figures S3A-S3D) and evaluated the CD4 effect on CXCR4 homodimer conformation. CD4 co-expression altered CXCR4 homodimers by reducing  $FRET_{max}$ , a parameter linked to total complex numbers (FRET  $_{max}$  for CXCR4/CXCR4, 0.6957  $\pm$  0.018;

# Figure 2. CXCL12 Binding **CXCR4 Dynamics and Enhances Receptor** Nanoclustering

(A-F) SPT analysis of CXCR4-AcGFP in JKCD4 cells on fibronectin (FN) or FN+CXCL12-coated coverslips

(A) Diffusion coefficient (D<sub>1-4</sub>) of single trajectories, with median (red line: 427 trajectories in 23 cells plated on FN, 424 trajectories in 24 cells on FN+ CXCL12 [n = 3; \*p  $\leq$  0.05]).

(B) Percentage of mobile and immobile trajectories at the cell membrane (593 in 23 cells on FN; 651 in 24 cells on FN<sup>+</sup>CXCL12 [n = 3, \*\*p  $\leq$  0.001]).

(C) Percentage of receptors/particle (595 trajectories in 23 cells on FN, 673 in 24 cells on FN+ CXCL12 [n = 5]).

(D) Percentage of mobile and immobile particles analyzed as in (B), as a function of particle size (monomer, 1; dimer, 2; nanocluster, ≥3 receptors/particle).

(E) Percentage of single-particle trajectories from CXCL12-stimulated cells, classified by type of motion using MSS analysis (254 in 24 cells; n = 3). (F) D<sub>1-4</sub> of individual trajectories with confined (left) or free (right) motion associated with size. (\*p  $\leq$ 0.05, \*\*p  $\leq 0.001$ ).

(G and H) Representative STED images of CXCR4 on CXCL12-activated Jurkat CD4+ cells (G) and T cells (H), with zoom of specific membrane regions (red square). Bar. 1 um. Probability distribution of number of receptors/spot (bottom) for both cell types, in steady state (gray) and post-CXCL12 stimulation (blue) (1,446 individual spots for Jurkat CD4+ cells and 1,849 for T cells, 30 cells in n = 2-3 STED experiments) is shown. See also Figure S2 and Movies S3 and S4.

 $CXCR4/CXCR4^{+}CD4$ , 0.5462 ± 0.032), without modifying FRET<sub>50</sub> values, that is, the apparent affinity between the two CXCR4 partners (CXCR4/CXCR4,  $0.5908 \pm 0.037$ ; CXCR4/CXCR4+CD4,  $0.6430 \pm 0.097$ ) (Figures 3A and 3B).

To study the influence of CD4 expression on CXCR4 clustering and lateral

diffusion, we generated SPT trajectories of CXCR4-AcGFP transiently transfected in Jurkat CD4+ cells and in Jurkat cells without CD4 expression (JK). Unstimulated JK cells showed a higher percentage of basal nanoclusters and fewer monomers and dimers compared to JKCD4 cells (Figures 3C and S3E). Ligand-induced larger nanoclustering was nonetheless very similar in both cell types (Figure S3F). siRNA downregulation of the receptor before CXCR4-AcGFP transfection (JK- cells) did not affect the degree of basal nanoclustering (Figure S3G). CXCL12 stimulation of these cells nonetheless increased the percentage of the largest nanoclusters (6-8 receptors/particle) relative to JKCD4 cells (Figures 3D and S2C). Our results indicate that CD4 co-expression reduces the percentage of basal CXCR4 nanoclusters in steady state.

We analyzed receptor mobility on JK and JKCD4 cells, before and after ligand stimulation. While no differences in D<sub>1-4</sub> values

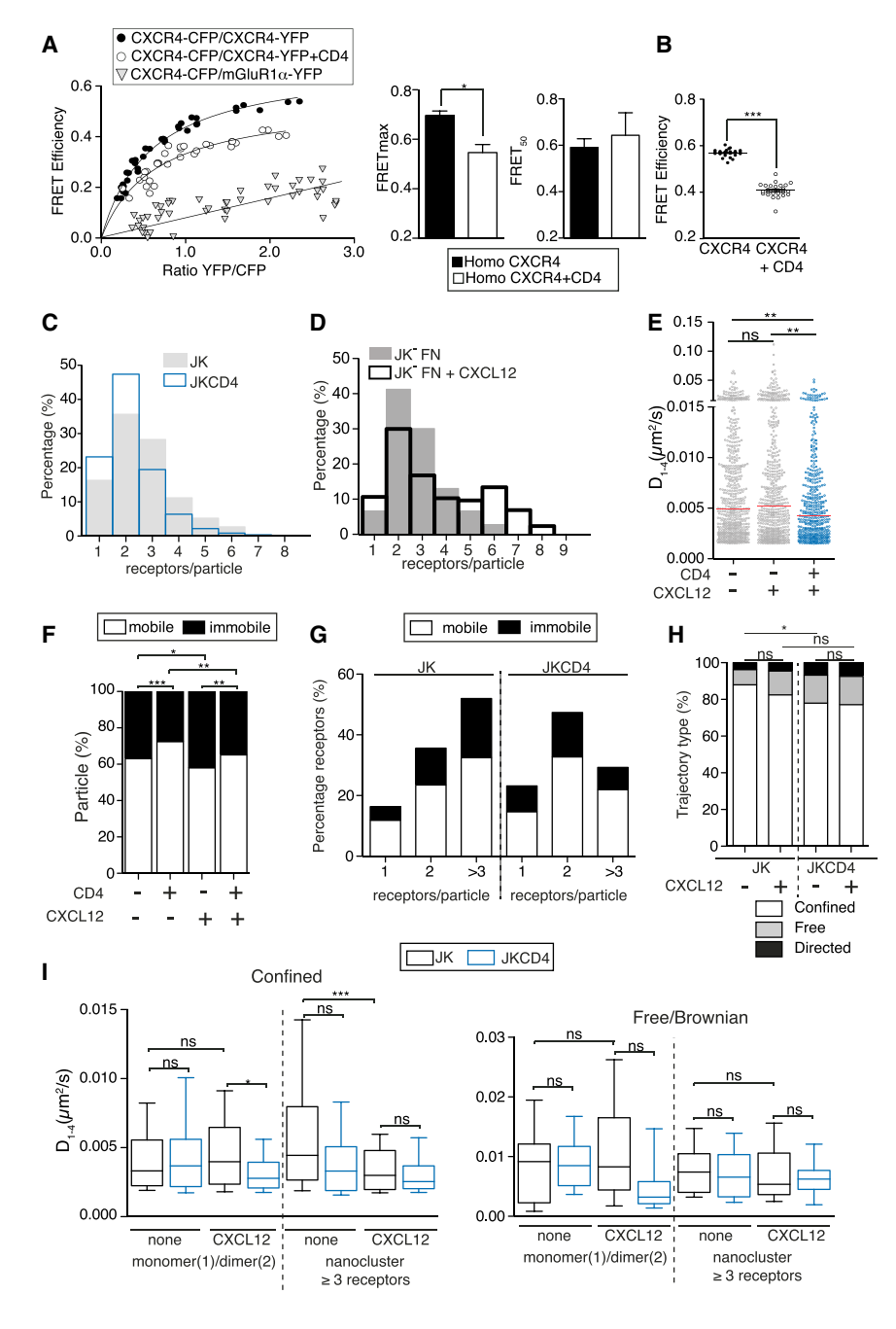


Figure 3. CD4 Co-expression Reduces CXCL12-Mediated CXCR4 Nanoclustering and Influences Its Lateral Diffusion

CD4 co-expression alters homodimeric CXCR4 conformation. FRET saturation curves were generated using 293T or 293CD4 cells transiently cotransfected with a constant amount of CXCR4-CFP and increasing amounts of CXCR4-YFP or of mGluR1α-YFP as negative control.  $FRET_{max}$  and  $FRET_{50}$  values (mean  $\pm$  SEM) were calculated using a nonlinear regression equation for a single binding-site model with a 95% confidence interval (n = 5; \*p  $\leq$  0.05). For the CXCR4/ mGluR1α negative control, the data fitted a linear regression (n = 3).

(B) FRET efficiency was evaluated using cells as in (A) transiently cotransfected at a fixed 1:1 CXCR4-YFP:CXCR4-CFP ratio. Data show mean ± SD  $(n = 3; ***p \le 0.0001).$ 

(C) Percentage of receptors/particle in steadystate JK and JKCD4 cells (937 and 595 trajectories, respectively, in 25 cells from n = 3-5).

(D) Effect of endogenous CXCR4 downregulation on percentage of receptors/particle in unstimulated and CXCL12-stimulated JK<sup>-</sup> cells (595 trajectories in 10 unstimulated cells and 507 in 8 CXCL12stimulated cells, n = 5).

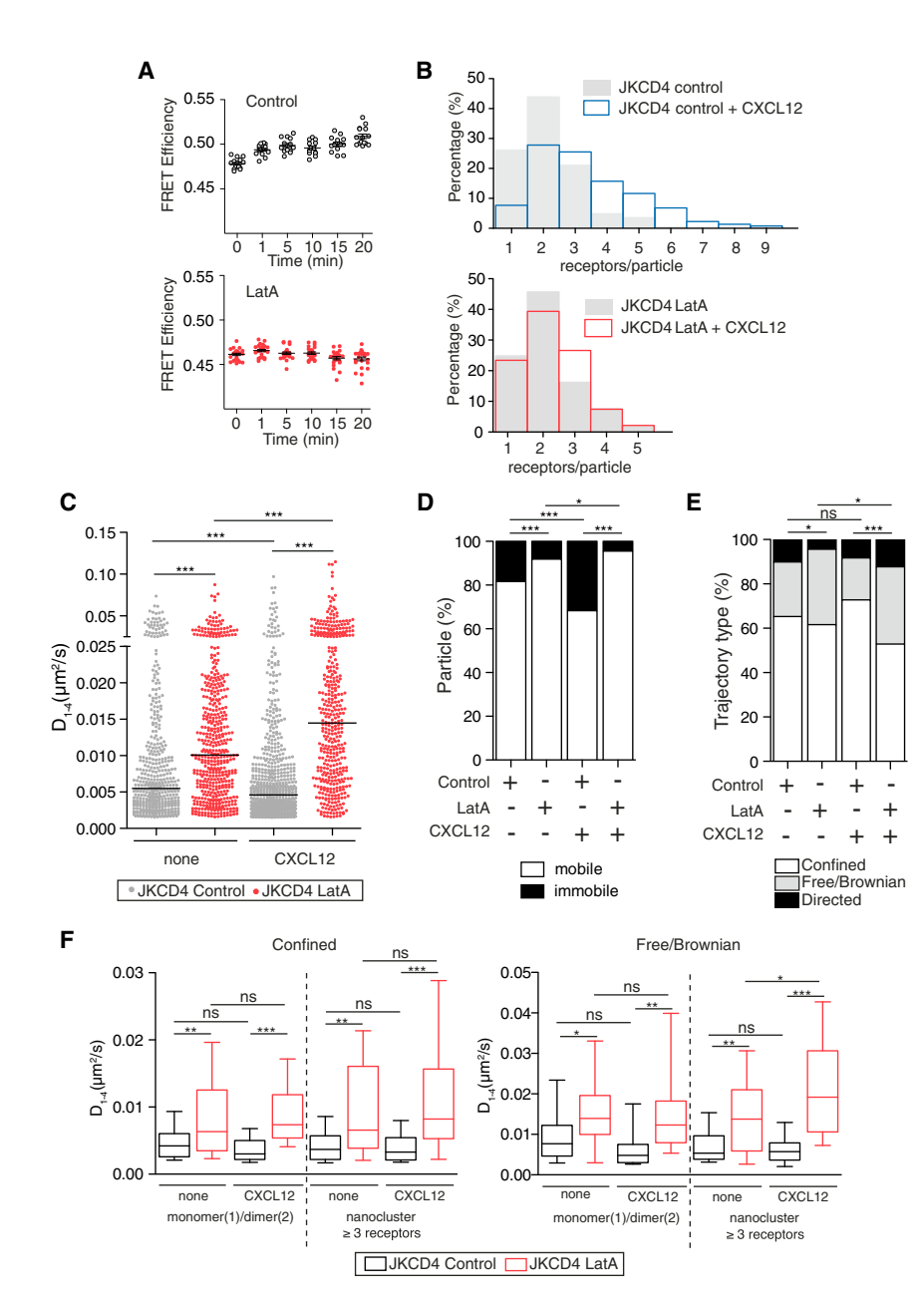
(E) D<sub>1-4</sub> CXCR4 distributions on JK and JKCD4 cells, steady state and CXCL12 stimulated, with median (red line) (564 trajectories in 10 unstimulated JK cells; 541 in 20 CXCL12-stimulated JK cells; 424 in 24 CXCL12-stimulated JKCD4 cells  $[n = 3-5; **p \le 0.001]$ ).

(F) Percentage of receptor trajectories, mobile or immobile, in steady state or after CXCL12 stimulation of JK and JKCD4 cells (894 trajectories in steady state; 933 after CXCL12 stimulation; data for 9–24 cells  $[n = 3, *p \le 0.05, **p \le 0.001, ***p \le 0.001]$ 0.0001]). To facilitate comparison, data for JKCD4 cells in Figure 2B are shown here.

(G) Percentage of mobile and immobile trajectories analyzed as in (F), as a function of particle size in JK and JKCD4 cells. For comparison, data for unstimulated JKCD4 cells in Figure 2D (left) are shown. (H) Percentage of mobile receptor trajectories classified as confined, free or directed for JK and JKCD4 cells in steady state or after CXCL12 stimulation (in JK cells, 290 trajectories for steady state and 307 for CXCL12 stimulated; in JKCD4 cells, 192 for steady state and 254 for CXCL12 stimulated [10–24 cells; n = 3–5; \*p  $\leq$  0.05]). For comparison, Figures 1F (steady-state JKCD4 cells) and 2E (CXCL12 stimulated) are shown.

(I) D<sub>1-4</sub> of single particles with confined or free motion associated with size, in steady state or CXCL12 stimulated, in JK and JKCD4 cells (\*p  $\leq$  0.05, \*\*\*p  $\leq$ 0.0001). For comparison, data for JKCD4 cells in Figure 2F are shown. See also Figure S3.

were observed in JK cells regardless of stimulation, receptor diffusion was slower in activated JKCD4 compared to JK cells (Figure 3E). Although this effect was modest, CD4 co-expression significantly increased the percentage of mobile receptors in basal and in activated cells (Figure 3F); this effect was more prominent in CXCR4 basal nanoclusters (Figure 3G). In steady state, JK cells showed an increase in the percentage of confined particles (~10%), and a reduced percentage of particles with free and directed motions compared to JKCD4 cells. After ligand activation, both cell types showed similar mobile trajectories (Figure 3H), but monomers and dimers diffused more rapidly in ligand-activated JK than in JKCD4 cells, regardless of diffusion type, confined or free (Figure 3I). CXCR4 dynamics was similar in JK cells, although the diffusion coefficient of confined nanoclusters was unaltered by ligand activation (Figures S3H-S3J). These observations further imply that, through interaction with



CXCR4, CD4 promotes a small but significant reduction in the encounter rate of small CXCR4 particles, which alters their lateral diffusion and affects CXCR4 nanocluster formation.

# **Cortical Actin Cytoskeleton Is Critical for CXCL12-Induced CXCR4 Clustering and Spatiotemporal Organization**

By acting as a fence, the actin cytoskeleton regulates plasma membrane compartmentalization and membrane protein dynamics (Plowman et al., 2005; Torreno-Pina et al., 2016). Actin dynamics also has an essential role in coordinating chemokine receptor signaling (Nishita et al., 2002). We used FRET on cells treated with latrunculin A (LatA) to block F-actin polymerization, or with nocodazole to inhibit microtubule dynamics, and evalu-

## Figure 4. Latrunculin A Treatment Blocks **CXCL12-Mediated Enhanced Nanocluster**ing and Increases CXCR4 Diffusion

(A) FRET efficiency of 293T cells transiently transfected at a fixed 1:1 CXCR4-YFP:CXCR4-CFP ratio were treated with LatA or ethanol (diluent) as control and stimulated with CXCL12 at different times (n = 3). Data are shown as mean ±

(B) Percentage of receptors/particle before (control) and after LatA treatment, for steady-state and CXCL12-stimulated JKCD4 cells (steady-state control, 451 trajectories in 13 cells; steady-state LatA. 467 in 16 cells: CXCL12-stimulated control. 282 in 13 cells; CXCL12-stimulated LatA, 662 trajectories in 15 cells [n = 3]).

(C) D<sub>1-4</sub> distributions for indicated conditions (median, black line; trajectory data as in B; n = 3; \*\*\* $p \le 0.0001$ ).

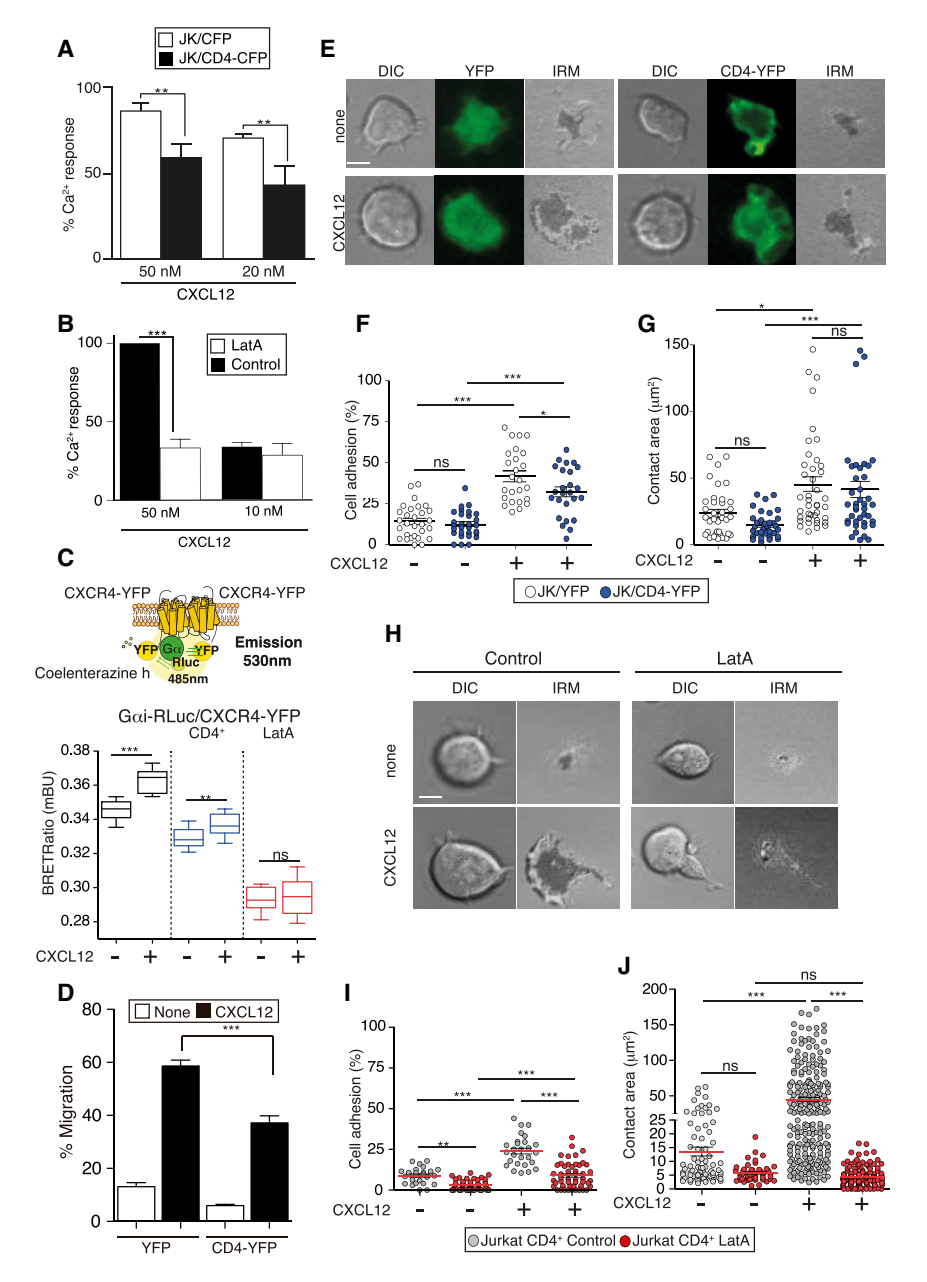
(D) Percentage of mobile and immobile particles for indicated conditions (steady-state control, 554 trajectories; steady-state LatA, 528; CXCL12stimulated control, 977; CXCL12-stimulated LatA, 425 [n = 3, \*p  $\leq$  0.05, \*\*\*p  $\leq$  0.0001]).

(E) Percentage of confined, free, and directed single-particle trajectories for indicated conditions (steady-state control, 236; steady-state LatA, 159; CXCL12-stimulated control, 434; CXCL12-stimulated LatA, 138 [n = 3; \*p  $\leq$  0.05, \*\*\*p  $\leq$  0.0001]). (F) D<sub>1-4</sub> of single particles with confined or Brownian/free motion associated with particle size, in steady state or CXCL12 stimulated, in JKCD4 cells pretreated with LatA or ethanol (control) (\*p < 0.05, \*\*p  $\leq 0.001$ , \*\*\*p  $\leq 0.0001$ ). See also Figure S4.

ated their influence on CXCR4 dimerization. In unstimulated cells, LatA did not affect FRET<sub>max</sub> or FRET<sub>50</sub> values but reduced the CXCL12-triggered increase in FRET<sub>max</sub> values (Figure S4A) and abolished the CXCL12-mediated increase in FRET efficiency (Figure 4A).

We used SPT on JKCD4 cells to test whether the actin cytoskeleton and/or the tubulin network modulate CXCR4 cluster size and lateral mobility. In steady

state, neither LatA nor nocodazole modified basal CXCR4 nanoclustering. LatA treatment abrogated CXCL12-mediated nanoclustering (Figure 4B), increased CXCR4 particle mobility (Figure 4C), and promoted a significant reduction in immobile particles; these effects were more pronounced after CXCL12 stimulation (Figure 4D). LatA reduced the percentage of confined particles and increased the number of CXCR4 particles with free motion (Figure 4E). LatA treatment also increased D<sub>1-4</sub> values, independently of particle trajectory (confined or free) or size (Figure 4F). Neither CXCR4 nanocluster size nor dynamics were affected by nocodazole (Figures S4B and S4C); its weak effect on D<sub>1-4</sub> values was due to DMSO, used as solvent (Figure S4D) (Gurtovenko and Anwar, 2007). We nonetheless observed that nocodazole abrogated CXCL12-mediated direct transport of



CXCR4 (Figure S4E), which suggests that, although there might be vesicle trafficking, it constitutes only a very small fraction of the trajectories analyzed. These findings indicate an important function for the actin cytoskeleton in spatiotemporal regulation of CXCR4. Whereas the actin cytoskeleton has no influence on the degree of basal CXCR4 nanoclustering, it affects its mobility. Indeed, ligand-mediated CXCR4-enhanced nanoclustering and lateral mobility are strongly dependent on the actin cytoskeleton.

# **CXCR4 Cluster Size Influences CXCL12-Mediated Functions**

Our data indicated that both CD4 co-expression and LatA treatment reduce CXCR4 nanocluster size and alter receptor dy-

Figure 5. CD4 Co-expression and Cortical Actin Cytoskeleton Influence T Cell Function

(A) CXCL12-mediated Ca2+ flux in JK/CD4-CFP or JK/CFP cells. Data are shown as mean  $\pm$  SD (n = 3, \*\* $p \le 0.001$ ).

(B) CXCL12-mediated Ca2+ flux in Jurkat CD4+ cells pretreated with LatA or ethanol. Data are shown as mean  $\pm$  SD (n = 3, \*\*\*p  $\leq$  0.001).

(C) Scheme of BRET experiment to evaluate the effect of CD4 co-expression and LatA treatment on CXCL12-triggered conformational change of the CXCR4-Gal complex. 293T or 293CD4 cells expressing a fixed Gai-Rluc:CXCR4-YFP ratio were untreated or LatA pretreated and CXCL12 activated. Plot shows CXCR4-Gai conformational change as BRET ratio (mBU) efficiency promoted by CXCL12 stimulation. Data are shown as mean  $\pm$  SD (n = 3; \*\*p  $\leq$  0.001, \*\*\*p  $\leq$ 0.0001)

(D) JK/YFP or JK/CD4-YFP cell migration in response to 20 nM CXCL12. Data are shown as mean  $\pm$  SD (n = 5; \*\*\*p  $\leq$  0.0001).

(E) Representative differential interference contrast (DIC), YFP fluorescence, and interference reflection microscopy (IRM) images of JK/YFP and JK/CD4-YFP cells in basal conditions (none) or CXCL12 stimulated. Bar, 5 µm.

(F) Adhesion frequency of JK/YFP and JK/CD4-YFP cells to ICAM-1-containing lipid bilayers, alone or CXCL12 coated. Each dot represents an image field with 20-40 cells (mean  $\pm$  SEM, n = 3,  $p \le 0.05, p \le 0.0001$ .

(G) Contact area (μm²) of cells in (F) estimated from IRM images (mean  $\pm$  SEM, n = 3, \*p  $\leq$  0.05, \*\*\*p  $\leq$ 0.0001).

(H) Representative DIC and IRM images of Jurkat CD4+ cells pretreated with LatA or ethanol (control). Bar, 5 µm.

(I) Adhesion frequency of LatA- or ethanol-pretreated Jurkat CD4+ cells to ICAM-1- or ICAM-1+CXCL12-containing lipid bilayers (mean ± SEM, n = 3; \*\* $p \le 0.001$ , \*\*\* $p \le 0.0001$ ).

(J) Contact area (µm2) of cells in (I) estimated from IRM images (mean  $\pm$  SEM, n = 3; \*\*\*p  $\leq$  0.0001). See also Figure S5.

namics at the cell membrane, although with distinct effectiveness. We thus evaluated CXCL12-triggered Ca2+ flux in Ju-

rkat cells transiently transfected with CD4-CFP (JK/CD4-CFP) or with the CFP control plasmid (JK/CFP). Both cell types expressed similar CXCR4 levels (Figure S5A). CD4 co-expression significantly reduced CXCL12-triggered Ca2+ flux (Figure 5A), and LatA treatment reduced CXCL12-mediated Ca2+ mobilization in Jurkat CD4+ and in T cells (Figures 5B and S5B). Since CD4 co-expression and LatA treatment interfere with CXCR4 nanocluster size, these data suggest that CXCL12-mediated Ca<sup>2+</sup> flux was affected by receptor nanoclustering.

We used bioluminescence resonance energy transfer (BRET) to study the relationship between nanocluster size and CXCL12 ability to activate Gai. In HEK293T (293T) cells cotransfected with Gα<sub>i</sub>-Rluc and CXCR4-YFP (Figure S5C), the CXCL12-mediated conformational change in the CXCR4/Gai complex was altered by CD4 co-expression, which was more efficient after F-actin polymerization blockade (Figure 5C). Jurkat cells transiently transfected with CD4-YFP (JK/CD4-YFP) migrated less toward CXCL12 gradients than empty vectortransfected Jurkat cells (JK/YFP) (Figure 5D). In a 2D lipid bilayer system with embedded ICAM-1 (intercellular adhesion molecule 1), alone or with CXCL12, JK/CD4-YFP cells adhered less than JK/YFP cells, although cell contact area with the substrate did not differ (Figures 5E-5G). CXCL12-mediated adhesiveness to ICAM-1 was greatly reduced in LatA-treated versus untreated Jurkat CD4+ cells, and the cell contact area was also smaller (Figures 5H-5J). Although many factors affect cell adhesion (Parsons et al., 2010), our results strongly suggest that modulating CXCR4 nanocluster size allows alteration of receptor-associated function.

# K239, V242, and L246 Residues in TMVI Are Essential for CXCR4 Clustering

The CXCR4 crystal structure shows a homodimer whose interface is located in the transmembrane regions (Wu et al., 2010). We thus predicted that oligomers are complexes formed by dimeric entities and used in silico analysis to determine the residues in the CXCR4 TM regions involved in receptor oligomerization that do not alter receptor homodimers. We identified several transmembrane peptides in TMIV, TMV, TMVI, and TMVII (Figure 6A), which we screened for their ability to antagonize CXCL12-mediated cell migration. The CXCR4 TMVI-based peptide <sup>239</sup>KPTVILILA<sup>247</sup> (<sup>239</sup>TMVI), which blocked CXCL12-mediated Jurkat CD4+ cell migration (Figure 6B), was selected for further study. The remaining peptides did not alter CXCR4-mediated functions, confirming specificity of the effect. In an additional control, 239TMVI treatment did not affect CXCL13- or CCL21-induced migration of cells that do not express endogenous CXCR4 (KG1a cells), which were transiently transfected with CXCR5 or CCR7, respectively (Figure S6A), The TMV synthetic peptide <sup>221</sup>IIISKLSH<sup>228</sup> (<sup>221</sup>TMV) was used as control for later experiments (Figure 6B). 239 TMVI treatment promoted a significant increase in the FRET efficiency of CXCR4 homodimers, which confirmed CXCR4 interaction without disrupting homodimeric complexes. Control 221TMV treatment did not modify basal FRET efficiency (Figure 6C). Both peptides were incorporated into the cell membrane, as shown by flow cytometry using biotin-labeled peptides (Figure S6B). In TIRF assays of JKCD4 cells, we observed that <sup>239</sup>TMVI specifically blocked CXCL12mediated CXCR4 nanoclustering (Figure 6D).

We next identified *in silico* the <sup>239</sup>TMVI amino acid residues with side chains on the outer side of the receptor complex (Figure 6E). We generated a triple-point mutant (K239E, V242A, and L246A substitutions) in the theoretical contact region of CXCR4 oligomers (Figure 6E). In transiently transfected JKCD4 cells with CXCR4mut-AcGFP (JKCD4 mut) and wild-type (WT) CXCR4-AcGFP (JKCD4 WT), anti-CXCR4 staining showed that both receptors were expressed equally at the cell membrane (Figure S6C) and bound CXCL12 (CXCR4wt dissociation constant (K<sub>D</sub>): 0.60 nM, CXCR4mut K<sub>D</sub>: 0.62 nM) and were internalized similarly in response to the ligand (Figure S6D). They formed homo- and heterodimers, as shown by FRET analysis

in 293T cells (Figure 6F). Both homodimers showed similar FRET<sub>50</sub> values, which indicated that their respective protomers bound with similar apparent affinity (Table S1). The FRET<sub>max</sub> value for CXCR4mut homodimers was nonetheless significantly lower, which suggested a larger number of CXCR4wt homodimeric complexes (Figure 6F; Table S1), or the presence of large nanoclusters that also affect FRET efficiency (James et al., 2006).

Analysis of SPT trajectories on Jurkat CD4<sup>+</sup> cells transfected with CXCR4-AcGFP (JKCD4 WT) or with CXCR4mut-AcGFP (JKCD4 mut) indicated that, in steady state, CXCR4mut particle size was similar to that of CXCR4wt (Figure 6G). In contrast, whereas CXCL12 promoted CXCR4wt nanoclustering (~70% nanoclusters, ≥3 receptors/particle), the effect on CXCR4mut was greatly reduced (~30% nanoclusters) (Figure 6H). In JK-CD4 mut cells, the reduction in nanocluster size was even greater despite CXCL12 activation; nanoclustering was largely abolished and >94% of particles were monomers/dimers (Figure 6H). The ability of CXCR4mut and CXCR4wt to heterodimerize could explain these cell-dependent differences. We found no change in the type of motion between the two receptors (Figure S6E), or variation in the CXCR4mut diffusion coefficient between cells with or without endogenous CXCR4 expression (Figure 6I). In the absence of endogenous CXCR4, ≥90% of CXCR4mut particles were mobile (Figure 6J). These data indicate that K239, V242, and L246 participate in CXCR4 nanoclustering.

# **CXCR4 Nanoclusters Are Essential for Cell Migration**

To determine the functional effects of CXCR4 nanoclustering, we evaluated  $G\alpha_i$  protein activation by CXCR4mut. Immunoprecipitation and immunoblot analysis showed that CXCR4wt and CXCR4mut associated with  $G\alpha_i$  in response to CXCL12 (Figure 7A). BRET measurements showed that both receptors were constitutively associated with  $G\alpha_i$  (Figures 5C and 7B). Nonetheless, whereas CXCL12 binding to CXCR4wt promoted a conformational change in the CXCR4/ $G\alpha_i$  complex compatible with signaling cascade activation (Figure 5C), we observed no marked changes when CXCL12 bound CXCR4mut (Figure 7B).

CXCL12 also promoted intracellular Ca<sup>2+</sup> flux in CXCR4wt-and in CXCR4mut-expressing cells, although responses via CXCR4mut were significantly lower (Figure 7C). CXCL12-mediated activation of MAPK (ERK1,2) and Pl3K (Akt) was notably compromised in CXCR4mut-expressing cells (Figure 7D), and cell migration toward CXCL12 was thus impaired (Figure 7E). Using the lipid bilayer system with embedded ICAM-1 plus CXCL12, we found that JK<sup>-</sup>CD4 mut cells did not migrate, showed defective substrate adhesion, and had a smaller contact area. In contrast, JK<sup>-</sup>CD4 WT cells were polarized, with a flattened leading-edge extension, and migrated across the lipid bilayer (Figures 7F and 7G; Movies S5 and S6). Receptor nanoclusters are thus needed for complete CXCR4 activation, although non-clustered receptors are able to promote ligand-mediated Ca<sup>2+</sup> flux.

To determine the *in vivo* relevance of CXCL12-mediated CXCR4 nanoclustering, we used a model of senescent neutrophil clearance to bone marrow, which depends on the CXCR4/CXCL12 axis (Furze and Rankin, 2008). Murine bone marrow

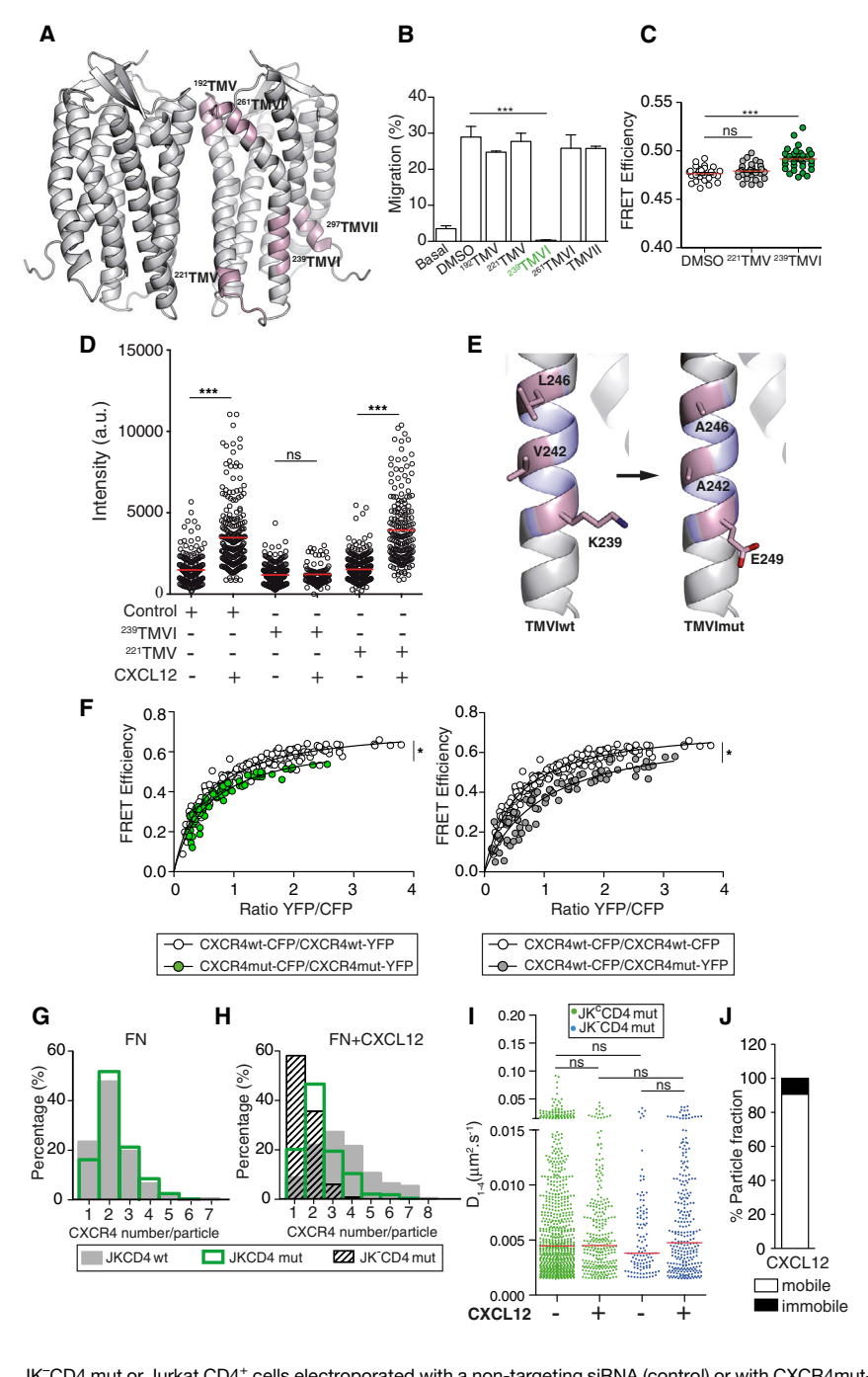


# Figure 6. CXCR4 Transmembrane Region VI Has a Key Role in Receptor Clustering

(A) Scheme of a CXCR4 homodimer modeled on the CXCR4 crystal structure (PDB: 3OE8), generated in the SWISS-MODEL server (https:// swissmodel.expasy.org/). Transmembrane regions predicted to be involved in CXCR4 oligomerization are shown in magenta.

(B) Jurkat CD4+ cells were preincubated with indicated peptides or the diluent (DMSO; control) and allowed to migrate (CXCL12). Data are shown as mean  $\pm$  SD (n = 5; \*\*\*p  $\leq$  0.0001).

(C) 293T cells, transiently cotransfected at a fixed 1:1 CXCR4-YFP:CXCR4-CFP ratio, were preincubated with DMSO or with peptides <sup>221</sup>TMV or <sup>239</sup>TMVI, and FRET efficiency was evaluated. Data are shown as mean  $\pm$  SD (n = 3, \*\*\*p  $\leq$  0.0001). (D) Intensity distribution (arbitrary units [a.u.]) from individual CXCR4 trajectories on unstimulated and CXCL12-stimulated JKCD4 cells, pretreated with 221 TMV, 239 TMVI, or DMSO (basal <sup>221</sup>TMV, 1,750 trajectories in 71 cells; basal <sup>239</sup>TMVI, 916 in 62 cells; basal control, 1,031 in 56 cells; CXCL12-stimulated <sup>221</sup>TMV, 1,157 in 58 cells; CXCL12-stimulated <sup>239</sup>TMVI, 1,104 in 59 cells; CXCL12-stimulated control, 1,200 in 48 cells). Mean is indicated (red) (n = 3; not significant, p > 0.05, \*\*\*p  $\leq$  0.0001).

(E) Left, residues in the TMVI region (stick representation; magenta) predicted to be involved in the CXCR4 nanoclustering interface (TMVIwt). Right, mutated residues (TMVImut).

(F) FRET saturation curves using 293T cells transiently cotransfected with a constant amount of CXCR4wt-CFP or CXCR4mut-CFP and increasing amounts of CXCR4wt-YFP or CXCR4mut-YFP. Data fitted to nonlinear regression equation assuming one binding site.  $\ensuremath{\mathsf{FRET}_{\mathsf{max}}}$  and  $\ensuremath{\mathsf{FRET}_{\mathsf{50}}}$ values were compared by an extra sum-ofsquares F test (n = 4-6. \*p < 0.05).

(G) Percentage of receptor/particle from unstimulated JKCD4 WT (595 trajectories in 22 cells, n = 3) and JKCD4 mut cells (996 in 24 cells; n = 3). For comparison, JKCD4 WT (from Figure 1I) is shown here.

(H) Cells as in (G) or JK-CD4 mut cells (hatched bars). Percentage of receptors/particle from CXCL12-stimulated cells (CXCR4wt, 669 trajectories in 24 cells; CXCR4mut, 420 in 22 cells; JK-CD4 mut, 392 in 22 cells; n = 3). For comparison, JKCD4 WT and FN+CXCL12 (from Figure 2C) are shown here.

(I)  $D_{1-4}$  distribution of steady-state or CXCL12stimulated CXCR4 particles (median, red), using

JKCD4 mut or Jurkat CD4+ cells electroporated with a non-targeting siRNA (control) or with CXCR4mut-AcGFP (JKCD4 mut cells) (steady-state JKCD4 mut, 792 in 26 cells; steady-state JKCD4, 113 in 14 cells; CXCL12-stimulated JKCD4 mut, 281 in 22 cells; CXCL12-stimulated JKCD4 mut, 272 in 22 cells; n = 3). (J) Percentage of CXCR4 mobile and immobile trajectories (as in Figure 2B) in unstimulated JKCD4 mut cells (336 trajectories in 22 cells; n = 3). See also Figure S6 and Table S1.

neutrophils were stained with CellTracker green (CMFDA) and incubated with the <sup>239</sup>TMVI peptide, <sup>221</sup>TMV (control), or PTx as positive control of CXCR4 function blockade. We confirmed <sup>239</sup>TMVI antagonism in an in vitro chemotaxis assay of neutrophils to CXCL12 gradients (Figure 7H). Treated neutrophils were then injected intravenously into mice, and cell accumula-

tion in bone marrow was analyzed after 60 min by flow cytometry. Treatment with <sup>239</sup>TMVI inhibited neutrophil clearance by ~62%, whereas <sup>221</sup>TMV control peptide-treated neutrophils homed to bone marrow, as did controls (PBS- or DMSO-treated neutrophils). As a positive control of inhibition, PTx treatment inhibited clearance by  $\sim$ 46% (Figure 7I).

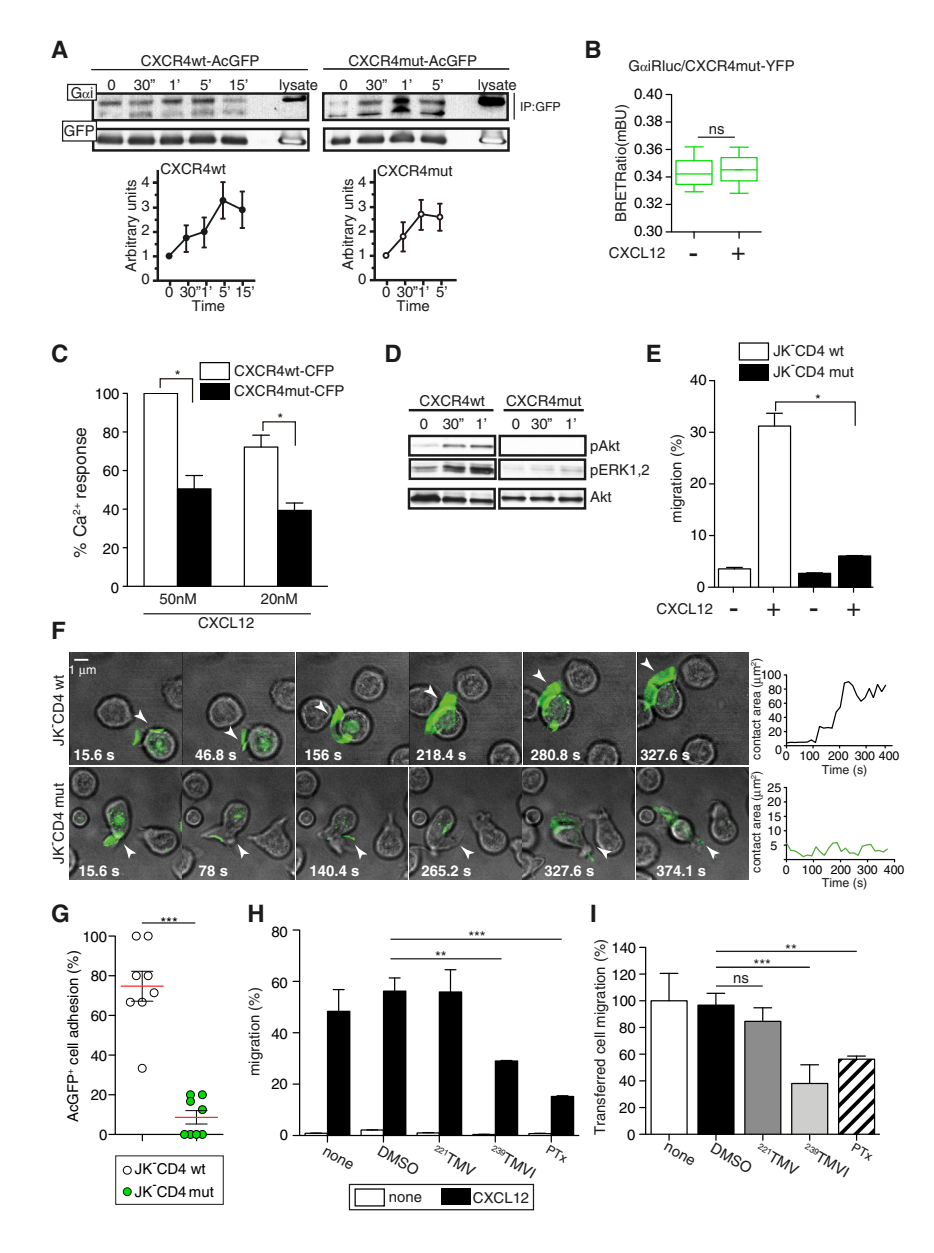


Figure 7. The Oligomerization-Deficient CXCR4 Mutant Receptor and the <sup>239</sup>TMVI Peptide Reduce CXCL12-Mediated Responses

- (A) Immunoblot analysis of Gα<sub>i</sub> protein association to CXCR4wt-AcGFP or CXCR4mut-AcGFPtransfected KG1a cells in response to CXCL12. Bottom, densitometry data with mean  $\pm$  SD (n = 3). (B) Unstimulated and CXCL12-stimulated 293T cells transiently cotransfected at a fixed Gai-Rluc:CXCR4mut-YFP ratio. Plot shows changes in BRET ratio efficiency (n = 3; not significant, p > 0.05).
- (C) Ca2+ flux response to CXCL12 in 293T cells transfected with CXCR4wt-CFP or CXCR4mut-CFP (mean  $\pm$  SD, n = 3; \*p  $\leq$  0.05).
- (D) Immunoblot analysis of pERK1/2 and -pAkt in response to CXCL12 in cells as in (A). Total Akt was used as loading control.
- (E) CXCL12-induced chemotaxis of JK-CD4 WT and JK-CD4 mut cells (mean  $\pm$  SD, n = 3; \*p  $\leq 0.05$ ).
- (F) Merged time-lapse (indicated in seconds) DIC and fluorescence images of representative JK-CD4 WT and JK-CD4 mut cells as in (E), on ICAM1-containing lipid bilayers coated with CXCL12. Arrowheads, monitored cells/condition. Profiles of cell contact area (µm2) were estimated by IRM.
- (G) Adhesion frequency of cells as in (F) to ICAM-1containing CXCL12-coated lipid bilayers (mean ± SEM, n = 3; \*\*\* $p \le 0.0001$ ).
- (H) CXCL12-induced migration of mouse neutrophils pretreated with <sup>221</sup>TMV, <sup>239</sup>TMVI, DMSO, or PTx (mean  $\pm$  SD, n = 3; \*\*p  $\leq$  0.001, \*\*\*p  $\leq$
- (I) Quantitation of adoptively transferred CMFDAlabeled neutrophils from bone marrow of recipient C57BL/6 mice 1 hr post-cell transfer. Before transfer, neutrophils were preincubated as in (H) (mean  $\pm$  SD, n = 3; \*\*p  $\leq$  0.001, \*\*\*p  $\leq$  0.0001). See also Movies S5 and S6.

#### **DISCUSSION**

The ability of chemokine receptors to dimerize is firmly established, but their lateral organization in the cell membrane, their potential coexistence with a fraction of apparent monomers, the presence of higher-order complexes (nanoclusters), and how this organization influences chemokine function remain largely unknown. Using SPT-TIRF and super-resolution microscopy we show that CXCR4 is organized at the cell membrane in non-clustered entities (monomers and dimers) and nanoclusters (groups of ≥3 receptors). Most CXCR4 molecules were temporarily confined in a region delimited by the F-actin cytoskeleton. In the presence of F-actin polymerization blockers, the freely diffusing receptor fraction increased. Moreover, the CD4 co-receptor significantly affected the mobility of CXCR4

monomer and dimer populations, thus regulating the final size of CXCL12dependent nanoclusters. These data

coincide with the reduced FRET<sub>max</sub> value in CD4-expressing cells, which might anticipate a reduction in oligomer numbers. CXCL12 binding enhanced receptor nanoclustering, with a significant reduction in monomers and dimers, and an increased percentage of the largest nanoclusters (10-18 receptors), which were generally immobile. GPCR ligands promote association of cytoplasmic signaling molecules to the receptor, which helps reduce receptor complex diffusion rates as well as their ability to move within the confinement regions (Cézanne et al., 2004; Jacquier et al., 2006). Receptor clustering increases cell sensitivity (Bray, 1995) but is also a means for efficient cell signal propagation (Cho and Stahelin, 2005) and increases the robustness of signaling systems (Gurry et al., 2009); its role in lymphocyte activation is widely reported (Depoil et al., 2008; Schamel et al., 2005).

Using the CXCR4 crystal structure as a model, we determined that three TMVI residues (K239, V242, L246) are essential for receptor nanoclustering. The CXCR4 triple mutant K239A/V242A/ L246A, which was expressed normally and formed homodimers with the same apparent affinity as CXCR4wt, did not form nanoclusters in steady state or after ligand activation. These data concur with the reduced  $FRET_{max}$  value in CXCR4mut, which also indicates a smaller number of CXCR4 nanoclusters. Our FRET data also showed a greater donor-acceptor distance (r) between protomers in CXCR4mut dimers (4.75 nm) compared to CXCR4wt complexes (4.55 nm). Given the larger size of CXCR4 clusters detected by SPT, some conformational changes might occur in the protomers that participate in these complexes, which would reduce acceptor-donor distance, thus increasing FRET signals.

The mutant receptor triggered Ca2+ flux after ligand binding. although to a much lesser extent compared to CXCR4wt. CXCL12-mediated ERK and AKT phosphorylation were also much lower, which reduced cell adhesion and migration. These results reveal a critical role for CXCR4 structural motifs in requlating its ligand-dependent nanoclustering capacity and underscore a strong relationship between receptor nanoclustering and the threshold necessary for receptor function. Although more modest, data for JKCD4 cells also indicated that CD4 modulates CXCR4 spatiotemporal distribution; this might explain the significant decrease in CXCL12-mediated cell adhesion to ICAM-1 and cell migration between Jurkat CD4+ and Jurkat cells. These data correlate with the role of CCR7 oligomerization in dendritic cell migration from inflammation sites to draining lymph nodes (Hauser et al., 2016).

To migrate, leukocytes reorganize their actin cytoskeleton to generate a protrusive leading edge and a contractile uropod (Nourshargh and Alon, 2014). Chemokine receptors concentrate at the leading edge, which facilitates detection of the chemotactic gradient formed in vivo by glycosaminoglycan-associated chemokine oligomers (Hoogewerf et al., 1997). We hypothesize that the increase in local chemokine concentration determines receptor nanoclustering and direction of cell movement. Receptor nanoclustering also allows the cell to localize its signaling machinery where needed to translate gradient sensing into cell movement.

Evidence shows that the actin cytoskeleton has key role in regulating membrane diffusion, protein compartmentalization and clustering, and in control of receptor signaling (Mattila et al., 2016). Our data suggest that the actin cytoskeleton is essential for ligand-mediated CXCR4 nanoclustering, needed to activate specific signaling pathways. A connection is reported between CXCR4 and actin through filamin A, drebrin, or moesin (Barrero-Villar et al., 2009; Gómez-Moutón et al., 2015; Moon et al., 2013). The precisely coordinated relationship between chemokines and the actin cytoskeleton promotes integrin activation (Smith et al., 2005), among other effects. In LatA-treated cells, we found reduced CXCL12-mediated adhesiveness to ICAM-1, which correlated with a smaller cell contact area with substrate. These findings indicate a central role for CXCL12mediated effects on actin polymerization in receptor nanoclustering and in chemokine-mediated integrin activation. Some reports show that chemokines transiently restrict integrin lateral mobility in T cells, and that this immobilization correlates with integrin activation and cell adhesion (Sosa-Costa et al., 2016). Our T cells that expressed the nanoclustering-deficient CXCR4 mutant did not adhere to a lipid bilayer with embedded ICAM1/ CXCL12, which indicates the need for receptor nanoclustering to trigger integrin activation. The connection between receptor nanoclusters and the actin cytoskeleton at the cell leading edge thus facilitates integrin activation and modulation of T lymphocyte motility.

Ligand binding to GPCR induces changes in receptor conformation that translate to downstream effector activation (Berchiche et al., 2007). After ligand binding, G proteins associate GPCR (Ritter and Hall, 2009). Our data nonetheless showed constitutive association between CXCR4 and Gai, with CXCL12 promoting a conformational change in the CXCR4/Gai complex compatible with signaling activation. BRET data also indicated constitutive association between Ga; and the mutant CXCR4. Although this receptor might be a conformational change-defective mutant, it is more likely that CXCL12 triggered a conformational change in CXCR4mut distinct from that induced in CXCR4wt, since CXCR4mut triggered some Ca2+ flux and was internalized after ligand activation. Specific ligand-mediated conformational changes in the receptor, which promote larger nanoclustering, might be necessary to recruit and activate the signaling molecules and would explain the lack of CXCR4mut function. This observation coincides with a recent model of separate signaling pathways for CCR7 oligomers (Hauser et al., 2016); G protein activation through the chemokine receptors seems insufficient for a complete response. We hypothesize a double conformational change in CXCR4 to trigger full function, one induced by ligand binding, sufficient to promote some Ca2+ flux and actin polymerization, and the other associated with nanoclustering and activation of the full set of signaling pathways needed for cell migration. A similar double conformational change in the receptor was used to explain JAK/STAT activation by IFN-γ, one triggered by ligand binding and the other by JAK activation (Blouin et al., 2016).

GPCR oligomerization is involved in ligand-mediated signaling, in protein trafficking to the cell membrane, and in internalization (Milligan, 2004). Our triple mutant CXCR4, which dimerizes but does not form large nanoclusters, is expressed at the cell membrane and is internalized similarly to the WT receptor. These data coincide with the model that chemokine receptors are delivered to the cell surface as dimers (Milligan, 2004) but rule out a need for clustering before internalization. CXCL12 stimulation increased the immobile CXCR4 fraction, and we detected >20% of nanoclusters formed by more than three receptors. Although we initially considered these nanoclusters as candidates for internalization, this idea was discarded, as the triple mutant was internalized in the absence of large nanoclusters; indeed, PitStop2-treated CXCR4wt cells showed similar percentages of large nanoclusters. We thus propose that rather than facilitating receptor internalization, these immobile nanoclusters allow correct positioning of the cell signaling machinery.

These results, obtained using high spatial resolution analysis in living cells, indicate that CXCR4 structural motifs are responsible for the basal nanoclustering of the receptor, crucial for formation of large nanoclusters after CXCL12 activation. Nanocluster size defines CXCR4 dynamics and thus its ability to trigger function. As a result, fine-tuning of monomer and dimer mobility affects CXCL12-dependent CXCR4 nanoclustering, signaling, and receptor function. We thus identify a synergistic role between receptor structural motifs and local organizers of the cell membrane to regulate CXCR4 spatiotemporal organization and function. This observation is highlighted by the finding that CXCR4 <sup>239</sup>TMVI peptides that intercalated between surrounding CXCR4 dimers abolished CXCL12-mediated large nanoclustering and thus the in vivo functions. These results will enable development of compounds that disassemble the CXCR4 molecular nanocluster and thus modulate its functions in the cell. As the CXCR4/CXCL12 axis is involved in many pathologies, drugs that alter the nanoclustering of this and perhaps of other chemokine receptors could improve current therapeutic approaches.

#### **STAR**\*METHODS

Detailed methods are provided in the online version of this paper and include the following:

- KEY RESOURCES TABLE
- CONTACT FOR REAGENT AND RESOURCE SHARING.
- EXPERIMENTAL MODEL AND SUBJECT DETAILS
  - O Cell lines and primary cells
  - Mice
- METHOD DETAILS
  - Antibodies
  - Reagents
  - $\, \bigcirc \,$  Fusion proteins and expression vectors
  - O Production of monomeric AcGFP protein
  - $\ \, \circ \ \, \mathsf{FRET} \mathsf{\, experiments} \\$
  - BRET
  - O Sample preparation for STED imaging
  - STED imaging
  - O STED image analysis
  - O Sample preparation for SPT
  - O Single-particle tracking (SPT) measurement
  - Single particle tracking analysis
  - O Minimum detectable diffusion coefficient
  - Trajectory analysis
  - $\ \, \bigcirc \ \, \text{Particle stoichiometry determination}$
  - Modeling of oligomeric CXCR4
  - Flow cytometry analysis
  - Calcium determination
  - Transwell migration assay
  - O Cell adhesion on planar lipid bilayers
  - O Western blot and co-immunoprecipitation
  - Biacore kinetics to measure K<sub>D</sub>
  - Adoptive transfer experiments
- QUANTIFICATION AND STATISTICAL ANALYSIS

#### SUPPLEMENTAL INFORMATION

Supplemental Information includes five figures, two tables, and six movies and can be found with this article online at https://doi.org/10.1016/j.molcel.2018.02.034.

#### **ACKNOWLEDGMENTS**

We thank Drs. M. Dustin (University of Oxford, UK) and J.V. Stein (Theodor Kocher Institute, Switzerland) for critical review of the manuscript. We thank C. Mark for editorial assistance. This work was supported by grants from the Spanish Ministry of Economy and Competitiveness (SAF 2014-53416-R, SAF 2017-82940-R AEI/FEDER, EU) and the RETICS Program (RD16/0012/0006; RIER), Ministry of Economy and Competitiveness, Severo Ochoa Programme for Centres of Excellence in R&D (SEV-2013-0347; SEV-2015-0522), and Fundación Privada Cellex and Generalitat de Catalunya (CERCA program). L.M.-M. is supported by the COMFUTURO program of the Spanish Research Council General Foundation.

#### **AUTHOR CONTRIBUTIONS**

L.M.-M., J.M.R.-F., and M.M. designed all aspects of the study; L.M.-M., J.M.R.-F., R.B., P.L., E.M.G.-C., and G.C. performed experiments; L.M.-M., L.B., and Y.R.C. performed adhesion experiments on lipid bilayers; C.A.S. modeled the crystal packing structure; C.O.S.S. and J.V. developed MATLAB scripts for automatic quantitation of TIRF images; J.A.T.-P., E.G., and C.M. developed some scripts for TIRF analysis and analyzed STED images; Y.R.C., F.S.-M., and M.F.G.-P. provided input into the project; L.M.-M., J.M.R.-F., M.F.G.-P., and M.M. wrote the manuscript.

#### **DECLARATION OF INTERESTS**

The authors declare no competing interests.

Received: July 5, 2017 Revised: January 8, 2018 Accepted: February 27, 2018 Published: April 5, 2018

#### REFERENCES

Ayoub, M.A., Maurel, D., Binet, V., Fink, M., Prézeau, L., Ansanay, H., and Pin, J.P. (2007). Real-time analysis of agonist-induced activation of protease-activated receptor 1/Galphai1 protein complex measured by bioluminescence resonance energy transfer in living cells. Mol. Pharmacol. 71, 1329–1340.

Baíllo, A., Martínez-Muñoz, L., and Mellado, M. (2013). Homogeneity tests for Michaelis-Menten curves with application to fluorescence resonance energy transfer data. J. Biol. Syst. *21*, 1350017.

Baker, A., Saulière, A., Dumas, F., Millot, C., Mazères, S., Lopez, A., and Salomé, L. (2007). Functional membrane diffusion of G-protein coupled receptors. Eur. Biophys. J. 36, 849–860.

Barrero-Villar, M., Cabrero, J.R., Gordón-Alonso, M., Barroso-González, J., Alvarez-Losada, S., Muñoz-Fernández, M.A., Sánchez-Madrid, F., and Valenzuela-Fernández, A. (2009). Moesin is required for HIV-1-induced CD4-CXCR4 interaction, F-actin redistribution, membrane fusion and viral infection in lymphocytes. J. Cell Sci. *122*, 103–113.

Berchiche, Y.A., Chow, K.Y., Lagane, B., Leduc, M., Percherancier, Y., Fujii, N., Tamamura, H., Bachelerie, F., and Heveker, N. (2007). Direct assessment of CXCR4 mutant conformations reveals complex link between receptor structure and G(alpha)(i) activation. J. Biol. Chem. 282, 5111–5115.

Bethani, I., Skånland, S.S., Dikic, I., and Acker-Palmer, A. (2010). Spatial organization of transmembrane receptor signalling. EMBO J. 29, 2677–2688.

Bleul, C.C., Farzan, M., Choe, H., Parolin, C., Clark-Lewis, I., Sodroski, J., and Springer, T.A. (1996). The lymphocyte chemoattractant SDF-1 is a ligand for LESTR/fusin and blocks HIV-1 entry. Nature *382*, 829–833.

Blouin, C.M., Hamon, Y., Gonnord, P., Boularan, C., Kagan, J., Viaris de Lesegno, C., Ruez, R., Mailfert, S., Bertaux, N., Loew, D., et al. (2016). Glycosylation-Dependent IFN- $\gamma$ R partitioning in lipid and actin nanodomains is critical for JAK activation. Cell *166*, 920–934.

Bray, D. (1995). Protein molecules as computational elements in living cells. Nature *376*, 307–312.

Brzostowski, J.A., Sawai, S., Rozov, O., Liao, X.H., Imoto, D., Parent, C.A., and Kimmel, A.R. (2013). Phosphorylation of chemoattractant receptors regulates chemotaxis, actin reorganization and signal relay. J. Cell Sci. 126, 4614–4626.

Calebiro, D., Rieken, F., Wagner, J., Sungkaworn, T., Zabel, U., Borzi, A., Cocucci, E., Zürn, A., and Lohse, M.J. (2013). Single-molecule analysis of fluorescently labeled G-protein-coupled receptors reveals complexes with distinct dynamics and organization. Proc. Natl. Acad. Sci. USA 110, 743-748.

Carrasco, Y.R., Fleire, S.J., Cameron, T., Dustin, M.L., and Batista, F.D. (2004). LFA-1/ICAM-1 interaction lowers the threshold of B cell activation by facilitating B cell adhesion and synapse formation. Immunity 20, 589-599.

Cézanne, L., Lecat, S., Lagane, B., Millot, C., Vollmer, J.Y., Matthes, H., Galzi, J.L., and Lopez, A. (2004). Dynamic confinement of NK2 receptors in the plasma membrane. Improved FRAP analysis and biological relevance. J. Biol. Chem. 279, 45057-45067.

Cho, W., and Stahelin, R.V. (2005). Membrane-protein interactions in cell signaling and membrane trafficking. Annu. Rev. Biophys. Biomol. Struct. 34,

Depoil, D., Fleire, S., Treanor, B.L., Weber, M., Harwood, N.E., Marchbank, K.L., Tybulewicz, V.L., and Batista, F.D. (2008). CD19 is essential for B cell activation by promoting B cell receptor-antigen microcluster formation in response to membrane-bound ligand. Nat. Immunol. 9, 63-72.

Destainville, N., and Salomé, L. (2006). Quantification and correction of systematic errors due to detector time-averaging in single-molecule tracking experiments. Biophys. J. 90, L17-L19.

Dorsch, S., Klotz, K.N., Engelhardt, S., Lohse, M.J., and Bünemann, M. (2009). Analysis of receptor oligomerization by FRAP microscopy. Nat. Methods 6, 225-230.

Eash, K.J., Greenbaum, A.M., Gopalan, P.K., and Link, D.C. (2010). CXCR2 and CXCR4 antagonistically regulate neutrophil trafficking from murine bone marrow. J. Clin. Invest. 120, 2423-2431.

Ewers, H., Smith, A.E., Sbalzarini, I.F., Lilie, H., Koumoutsakos, P., and Helenius, A. (2005). Single-particle tracking of murine polyoma virus-like particles on live cells and artificial membranes. Proc. Natl. Acad. Sci. USA 102, 15110-15115.

Furze, R.C., and Rankin, S.M. (2008). Neutrophil mobilization and clearance in the bone marrow. Immunology 125, 281-288.

Gómez-Moutón, C., Fischer, T., Peregil, R.M., Jiménez-Baranda, S., Stossel, T.P., Nakamura, F., and Mañes, S. (2015). Filamin A interaction with the CXCR4 third intracellular loop regulates endocytosis and signaling of WT and WHIM-like receptors. Blood 125, 1116-1125.

Griffith, J.W., Sokol, C.L., and Luster, A.D. (2014). Chemokines and chemokine receptors: Positioning cells for host defense and immunity. Annu. Rev. Immunol. 32, 659-702.

Gurry, T., Kahramanoğullari, O., and Endres, R.G. (2009). Biophysical mechanism for ras-nanocluster formation and signaling in plasma membrane. PLoS

Gurtovenko, A.A., and Anwar, J. (2007). Modulating the structure and properties of cell membranes: The molecular mechanism of action of dimethyl sulfoxide. J. Phys. Chem. B 111, 10453-10460.

Hamatake, M., Aoki, T., Futahashi, Y., Urano, E., Yamamoto, N., and Komano, J. (2009). Ligand-independent higher-order multimerization of CXCR4, a G-protein-coupled chemokine receptor involved in targeted metastasis. Cancer Sci. 100, 95-102.

Hansen, I.B., Ellingsen, T., Hornung, N., Poulsen, J.H., Lottenburger, T., and Stengaard-Pedersen, K. (2006). Plasma level of CXC-chemokine CXCL12 is increased in rheumatoid arthritis and is independent of disease activity and methotrexate treatment. J. Rheumatol. 33, 1754-1759.

Hauser, M.A., Schaeuble, K., Kindinger, I., Impellizzieri, D., Krueger, W.A., Hauck, C.R., Boyman, O., and Legler, D.F. (2016). Inflammation-induced CCR7 oligomers form scaffolds to integrate distinct signaling pathways for efficient cell migration. Immunity 44, 59-72.

Hoogewerf, A.J., Kuschert, G.S., Proudfoot, A.E., Borlat, F., Clark-Lewis, I., Power, C.A., and Wells, T.N. (1997). Glycosaminoglycans mediate cell surface oligomerization of chemokines. Biochemistry 36, 13570-13578.

Jacquier, V., Prummer, M., Segura, J.M., Pick, H., and Vogel, H. (2006). Visualizing odorant receptor trafficking in living cells down to the single-molecule level. Proc. Natl. Acad. Sci. USA 103, 14325-14330.

James, J.R., Oliveira, M.I., Carmo, A.M., Iaboni, A., and Davis, S.J. (2006). A rigorous experimental framework for detecting protein oligomerization using bioluminescence resonance energy transfer. Nat. Methods 3, 1001-1006.

Jagaman, K., and Grinstein, S. (2012). Regulation from within: The cytoskeleton in transmembrane signaling. Trends Cell Biol. 22, 515-526.

Jaqaman, K., Loerke, D., Mettlen, M., Kuwata, H., Grinstein, S., Schmid, S.L., and Danuser, G. (2008). Robust single-particle tracking in live-cell time-lapse sequences. Nat. Methods 5, 695-702.

Jaqaman, K., Kuwata, H., Touret, N., Collins, R., Trimble, W.S., Danuser, G., and Grinstein, S. (2011). Cytoskeletal control of CD36 diffusion promotes its receptor and signaling function. Cell 146, 593-606.

Kusumi, A., Nakada, C., Ritchie, K., Murase, K., Suzuki, K., Murakoshi, H., Kasai, R.S., Kondo, J., and Fujiwara, T. (2005). Paradigm shift of the plasma membrane concept from the two-dimensional continuum fluid to the partitioned fluid: High-speed single-molecule tracking of membrane molecules. Annu. Rev. Biophys. Biomol. Struct. 34, 351-378.

Ma, Q., Jones, D., Borghesani, P.R., Segal, R.A., Nagasawa, T., Kishimoto, T., Bronson, R.T., and Springer, T.A. (1998). Impaired B-lymphopoiesis, myelopoiesis, and derailed cerebellar neuron migration in CXCR4- and SDF-1-deficient mice. Proc. Natl. Acad. Sci. USA 95, 9448-9453.

Manzo, C., and Garcia-Parajo, M.F. (2015). A review of progress in single particle tracking: From methods to biophysical insights. Rep. Prog. Phys. 78,

Marino, K.A., Prada-Gracia, D., Provasi, D., and Filizola, M. (2016). Impact of lipid composition and receptor conformation on the spatio-temporal organization of  $\mu$ -opioid receptors in a multi-component plasma membrane model. PLoS Comput. Biol. 12, e1005240.

Martínez-Muñoz, L., Barroso, R., Dyrhaug, S.Y., Navarro, G., Lucas, P., Soriano, S.F., Vega, B., Costas, C., Muñoz-Fernández, M.A., Santiago, C., et al. (2014). CCR5/CD4/CXCR4 oligomerization prevents HIV-1 gp120IIIB binding to the cell surface. Proc. Natl. Acad. Sci. USA 111, E1960-E1969.

Mattila, P.K., Batista, F.D., and Treanor, B. (2016). Dynamics of the actin cytoskeleton mediates receptor cross talk: An emerging concept in tuning receptor signaling. J. Cell Biol. 212, 267-280.

McCorvy, J.D., and Roth, B.L. (2015). Structure and function of serotonin G protein-coupled receptors. Pharmacol. Ther. 150, 129-142.

Milligan, G. (2004). G protein-coupled receptor dimerization: Function and ligand pharmacology. Mol. Pharmacol. 66, 1–7.

Moertelmaier, M., Brameshuber, M., Linimeier, M., Schutz, G.J., and Stockinger, H. (2005). Thinning out clusters while conserving stoichiometry of labeling. Appl. Phys. Lett. 87, 263903.

Moon, Y., Kim, J.Y., Kim, W.R., Kim, H.J., Jang, M.J., Nam, Y., Kim, K., Kim, H., and Sun, W. (2013). Function of ezrin-radixin-moesin proteins in migration of subventricular zone-derived neuroblasts following traumatic brain injury. Stem Cells 31, 1696-1705.

Muñoz, L.M., Lucas, P., Holgado, B.L., Barroso, R., Vega, B., Rodríguez-Frade, J.M., and Mellado, M. (2011). Receptor oligomerization: A pivotal mechanism for regulating chemokine function. Pharmacol. Ther. 131, 351-358

Nishita, M., Aizawa, H., and Mizuno, K. (2002). Stromal cell-derived factor 1alpha activates LIM kinase 1 and induces cofilin phosphorylation for T-cell chemotaxis. Mol. Cell. Biol. 22, 774-783.

Nourshargh, S., and Alon, R. (2014). Leukocyte migration into inflamed tissues. Immunity 41, 694–707.

Palczewski, K. (2010). Oligomeric forms of G protein-coupled receptors (GPCRs). Trends Biochem. Sci. 35, 595-600.

Parsons, J.T., Horwitz, A.R., and Schwartz, M.A. (2010). Cell adhesion: Integrating cytoskeletal dynamics and cellular tension. Nat. Rev. Mol. Cell Biol. 11, 633–643.

Patra, M., Salonen, E., Terama, E., Vattulainen, I., Faller, R., Lee, B.W., Holopainen, J., and Karttunen, M. (2006). Under the influence of alcohol: The effect of ethanol and methanol on lipid bilayers. Biophys. J. 90, 1121–1135.

Plowman, S.J., Muncke, C., Parton, R.G., and Hancock, J.F. (2005). H-ras, K-ras, and inner plasma membrane raft proteins operate in nanoclusters with differential dependence on the actin cytoskeleton. Proc. Natl. Acad. Sci. USA 102, 15500–15505.

Ritter, S.L., and Hall, R.A. (2009). Fine-tuning of GPCR activity by receptor-interacting proteins. Nat. Rev. Mol. Cell Biol. *10*, 819–830.

Scarselli, M., Annibale, P., and Radenovic, A. (2012). Cell type-specific β2-adrenergic receptor clusters identified using photoactivated localization microscopy are not lipid raft related, but depend on actin cytoskeleton integrity. J. Biol. Chem. 287, 16768–16780.

Schamel, W.W., Arechaga, I., Risueño, R.M., van Santen, H.M., Cabezas, P., Risco, C., Valpuesta, J.M., and Alarcón, B. (2005). Coexistence of multivalent and monovalent TCRs explains high sensitivity and wide range of response. J. Exp. Med. 202, 493–503.

Schiraldi, M., Raucci, A., Muñoz, L.M., Livoti, E., Celona, B., Venereau, E., Apuzzo, T., De Marchis, F., Pedotti, M., Bachi, A., et al. (2012). HMGB1 promotes recruitment of inflammatory cells to damaged tissues by forming a complex with CXCL12 and signaling via CXCR4. J. Exp. Med. 209, 551–563.

Schmidt, T., Schütz, G.J., Gruber, H.J., and Schindler, H. (1996). Local stoichiometries determined by counting individual molecules. Anal. Chem. 68, 4397–4401.

Simson, R., Sheets, E.D., and Jacobson, K. (1995). Detection of temporary lateral confinement of membrane proteins using single-particle tracking analysis. Biophys. J. 69, 989–993.

Smith, A., Carrasco, Y.R., Stanley, P., Kieffer, N., Batista, F.D., and Hogg, N. (2005). A talin-dependent LFA-1 focal zone is formed by rapidly migrating T lymphocytes. J. Cell Biol. *170*, 141–151.

Sosa-Costa, A., Isern de Val, S., Sevilla-Movilla, S., Borgman, K.J., Manzo, C., Teixidó, J., and Garcia-Parajo, M.F. (2016). Lateral Mobility and Nanoscale Spatial Arrangement of Chemokine-activated  $\alpha 4\beta 1$  Integrins on T Cells. J. Biol. Chem. 291, 21053–21062.

Tachibana, K., Hirota, S., Iizasa, H., Yoshida, H., Kawabata, K., Kataoka, Y., Kitamura, Y., Matsushima, K., Yoshida, N., Nishikawa, S., et al. (1998). The chemokine receptor CXCR4 is essential for vascularization of the gastrointestinal tract. Nature *393*, 591–594.

Teicher, B.A., and Fricker, S.P. (2010). CXCL12 (SDF-1)/CXCR4 pathway in cancer. Clin. Cancer Res. 16, 2927–2931.

Thelen, M. (2001). Dancing to the tune of chemokines. Nat. Immunol. 2, 129-134.

Torreno-Pina, J.A., Manzo, C., Salio, M., Aichinger, M.C., Oddone, A., Lakadamyali, M., Shepherd, D., Besra, G.S., Cerundolo, V., and Garcia-Parajo, M.F. (2016). The actin cytoskeleton modulates the activation of iNKT cells by segregating CD1d nanoclusters on antigen-presenting cells. Proc. Natl. Acad. Sci. USA *113*, E772–E781.

van Zanten, T.S., Cambi, A., Koopman, M., Joosten, B., Figdor, C.G., and Garcia-Parajo, M.F. (2009). Hotspots of GPI-anchored proteins and integrin nanoclusters function as nucleation sites for cell adhesion. Proc. Natl. Acad. Sci. USA *106*, 18557–18562.

Veatch, S.L., Machta, B.B., Shelby, S.A., Chiang, E.N., Holowka, D.A., and Baird, B.A. (2012). Correlation functions quantify super-resolution images and estimate apparent clustering due to over-counting. PLoS ONE 7, e31457.

Vega, B., Muñoz, L.M., Holgado, B.L., Lucas, P., Rodríguez-Frade, J.M., Calle, A., Rodríguez-Fernández, J.L., Lechuga, L.M., Rodríguez, J.F., Gutiérrez-Gallego, R., and Mellado, M. (2011). Technical advance: Surface plasmon resonance-based analysis of CXCL12 binding using immobilized lentiviral particles. J. Leukoc. Biol. 90, 399–408.

Venkatesan, S., Rose, J.J., Lodge, R., Murphy, P.M., and Foley, J.F. (2003). Distinct mechanisms of agonist-induced endocytosis for human chemokine receptors CCR5 and CXCR4. Mol. Biol. Cell *14*, 3305–3324.

Vicente-Manzanares, M., and Sánchez-Madrid, F. (2004). Role of the cytoskeleton during leukocyte responses. Nat. Rev. Immunol. 4, 110–122.

Wu, B., Chien, E.Y., Mol, C.D., Fenalti, G., Liu, W., Katritch, V., Abagyan, R., Brooun, A., Wells, P., Bi, F.C., et al. (2010). Structures of the CXCR4 chemokine GPCR with small-molecule and cyclic peptide antagonists. Science *330*, 1066–1071.

Xu, J., Mora, A., Shim, H., Stecenko, A., Brigham, K.L., and Rojas, M. (2007). Role of the SDF-1/CXCR4 axis in the pathogenesis of lung injury and fibrosis. Am. J. Respir. Cell Mol. Biol. *37*, 291–299.

Zanacchi, F.C., Manzo, C., Alvarez, A.S., Derr, N.D., Garcia-Parajo, M.F., and Lakadamyali, M. (2017). A DNA origami platform for quantifying protein copy number in super-resolution. Nat. Methods *14*, 789–792.

Zimmermann, T., Rietdorf, J., Girod, A., Georget, V., and Pepperkok, R. (2002). Spectral imaging and linear un-mixing enables improved FRET efficiency with a novel GFP2-YFP FRET pair. FEBS Lett. *531*, 245–249.

Zou, Y.R., Kottmann, A.H., Kuroda, M., Taniuchi, I., and Littman, D.R. (1998). Function of the chemokine receptor CXCR4 in haematopoiesis and in cerebellar development. Nature *393*, 595–599.

# **STAR**\***METHODS**

# **KEY RESOURCES TABLE**

REAGENT or RESOURCE	SOURCE	IDENTIFIER
Antibodies		
Mouse monoclonal anti-CXCR4 (clone 44717)	R&D	Cat# MAB173
Mouse monoclonal anti-CXCR4 (clone 12G5)	R&D	Cat# FAB170B
Mouse monoclonal anti-CD4 (clone OKT-4)	eBioscience	Cat# 14-0048-82
Mouse monoclonal anti-Gαl (I-20)	Santa Cruz Biotechnology	Cat# sc-391
Mouse monoclonal anti-GFP (JL-8)	Clontech	Cat# 632381
Mouse monoclonal anti-p-ERK (E-4)	Santa Cruz Biotechnology	Cat# sc-7383
Rabbit polyclonal anti-p-Akt (Ser473)	Cell Signaling Technology	Cat# 9271
Rabbit polyclonal anti-Akt	Cell Signaling Technology	Cat# 9272
Donkey polyclonal anti-mouse IgG(H+L)-AF647- conjugated	Jackson Immunoresearch	Cat# A-31571
Goat polyclonal anti-mouse IgG(H+L)-AF488	Invitrogen	Cat# A-11029
Streptavidin-SPRD	Beckman Coulter	Cat# 733003
Bacterial and Virus Strains		
Escherichia coli: BL21(DE3)pLysS strain	Novagen	Cat# 69451
Biological Samples		
Buffy coats from healthy donors	Centro de Transfusiones de Madrid	http://www.madrid.org/cs/Satellite? language=es&pagename= CentrodeTransfusion%2FPage%2 FHLAV_home
Chemicals, Peptides, and Recombinant Proteins		
Latrunculin A	Sigma-Aldrich	Cat# 428021
Nocodazole	Sigma-Aldrich	Cat# M1404
Brefeldin A	Abcam	Cat# ab120299
PitStop2	Abcam	Cat# ab120687
PitStop2 negative control	Abcam	Cat# ab120688
Pertussis toxin from Bordetella pertussis (PTx)	Sigma-Aldrich	Cat# P2980
h-Coelenterazine	p.j.k.	Cat# 102181
Fibronectin human plasma	Sigma-Aldrich	Cat# F2006
1,2-dioleoyl-PC	Avanti Polar Lipids	Cat# 850375C
Fluo-3AM	Molecular Probes	Cat# F-1241
CellTracker Green CMFDA Dye	Thermo Fisher Scientific	Cat# C2925
Prolong Gold antifade Mountant	Thermo Fisher Scientific	Cat# P36930
Recombinant Humna CXCL12	PeproTech	Cat# 300-28A
Recombinant Human CCL21	PeproTech	Cat# 300-35
Recombinant Human CXCL13	PeproTech	Cat# 300-47
GPI-linked ICAM-1	Carrasco et al., 2004	N/A
Synthetic peptides, unlabeled or biotinylated (> 95% purity)	GenScript (Hong Kong)	https://www.genscript.com
Critical Commercial Assays		
Dynabeads Untouched Human CD4 T cells Kit	Thermo Fisher Scientific (Invitrogen DYNAL)	Cat# 11346D
Experimental Models: Cell Lines		
Human: HEK293T cells	ATCC	CRL-11268
Human: Jurkat cells	ATCC	CRL-10915
		(Continued on next page

(Continued on next page)

Continued		
REAGENT or RESOURCE	SOURCE	IDENTIFIER
Human: Jurkat CD4 <sup>+</sup> cells	Dr. J. Alcamí (Centro Nacional de Microbiología, ISCIII, Madrid, Spain)	N/A
Human: HEK293 CD4 (293CD4) cells	Dr. G. del Real (Instituto Nacional de Investigación y Tecnología Agraria y Alimentaria, Madrid, Spain)	N/A
Human: KG1a cells	Dr. J.Teixidó (Centro Investigaciones Biológicas/CSIC, Madrid, Spain)	ATCC: Cat# CCL-246.1
Human: primary heatlthy donor CD4 <sup>+</sup> T lymphocytes	This paper	N/A
Mouse: primary neutrophils	This paper	N/A
Experimental Models: Organisms/Strains		
Mouse: C57BL/6	Envigo	C57BL/6JJOlaHsd
Oligonucleotides		
Primer 5'HindIII to amplified CXCR4 and cloned into pECFP-N1, pEYFP-N1 and pAcGFP-N1: ATAAGCT TATGGAGGGGATCAGTATATACATTC	This paper	N/A
Primer 3'Agel to amplified CXCR4 and cloned into pECFP-N1, pEYFP-N1 and pAcGFP-N1: GACCGGTG GATCCCGTAAGCTGGAGTGAAAACTTGAAG	This paper	N/A
Primer 5'Xhol to cloned CD4 into pECFP-N1and pEYFP-N1: TTCTCGAGATGAACCGGGGAGTC CCTTTTAG	This paper	N/A
Primer 3'HindIII to cloned CD4 into pECFP-N1and pEYFP-N1: AAGCTTTAAAATGGGGCTACATGTCTTCTG	This paper	N/A
Primer 5'KpnI to cloned CD86 into pAcGFP-N1: AAGGTACCATGGATCCCCAGTGCACTATG	This paper	N/A
Primer 3'Agel to cloned CD86 into pAcGFP-N1: ACCGGTTTAAAACATGTATCACTTTTGTGC	This paper	N/A
Primers to generate the CXCR4 mutant: Fw:GGCG AAGAAAGCCGCGATGAGGATGGCTGTGGTCT CGAGGGCCTTGC	This paper	N/A
Rv:CGCAAGGCCCTCGAGACCACAGCCATCCT CATCGCGGCTTTCTTCGCC		
Primers to clone AcGFP monomeric into pET-22(+):	This paper	N/A
Fw Ndel: AACATATGGTGAGCAAGGGCGCCG		
Rv BamHI: GGATCCGAGCTGCCACGCGGAACCAG		
CTTGTACAGCTCATCCATGCC		
siRNA CXCR4 specific for the 3'UTR	Dharmacon	Cat# A-005139-14
Recombinant DNA		
pcDNA3.1-Gαi1	UMR cDNA Resource Center	IMAGE acc# Al246520 http://www. cdna.org
pRluc- Gαi1	This paper, based on Ayoub et al., 2007	N/A
pcDNA3.1-Gβ1	UMR cDNA Resource Center	http://www.cdna.org
pcDNA3.1-Gγ2	UMR cDNA Resource Center	http://www.cdna.org
pAcGFPm-N1 (PT3716-5)	Clontech	Cat# 632469
pECFP-N1 (PT3285-5)	Clontech	Cat# 6900-1
pEYFP-N1 (PT3192-5)	Clontech	Cat# 6006-1
pRLuc-N1	BioSignal Packard	Cat# 6310001
pET-22b(+)	Novagen	Cat# 69744-3
mGluR1α-YFP	Laboratory of Rafael Franco (Universidad Autónoma de Barcelona, Spain)	N/A
5HT <sub>2B</sub> -YFP	Laboratory of Rafael Franco (Universidad Autónoma de Barcelona, Spain)	N/A

(Continued on next page)

Continued		
REAGENT or RESOURCE	SOURCE	IDENTIFIER
Software and Algorithms		
MATLAB 2013a	The MathWorks, Natick,MA	http://www.mathworks.com/
U-Track2 software	Jaqaman et al., 2008	http://www.utsouthwestern.edu/labs/danuser/software/
Imaris 6.0 software	Bitplane	http://www.bitplane.com/
ImageJ 1.49v	ImageJ	https://imagej.nih.gov/ij/index.html
Pymol molecular graphics software	Schrödinger	https://pymol.org/2/
GraphPad PRISM 5.0	GraphPad Software	https://www.graphpad.com/
Others		
CM5 sensorchip	GE Healthcare BioSciences AB (Uppsala, Sweden)	Cat# BR-1000-12
Ficoll-paque plus	GE Healthcare BioSciences AB (Uppsala, Sweden)	Cat# 17-1440-03
Histopaque (density 1.077 mg/ml)	Sigma-Aldrich	Cat# 10771
Histopaque (density 1.119 mg/ml)	Sigma-Aldrich	Cat# 11191

#### CONTACT FOR REAGENT AND RESOURCE SHARING

Further information and requests for resources and reagents should be directed to and will be fulfilled by the Lead Contact, Mario Mellado (mmellado@cnb.csic.es).

#### **EXPERIMENTAL MODEL AND SUBJECT DETAILS**

#### **Cell lines and primary cells**

HEK293T (293T) cells were obtained from the American Type Culture Collection (CRL-11268). HEK293CD4 (293CD4), Jurkat CD4+ and KG1a cells were kindly donated by Drs. G. del Real (Instituto Nacional de Investigación y Tecnología Agraria y Alimentaria, Madrid, Spain), J. Alcamí (Centro Nacional de Microbiología, Inst Salud Carlos III, Madrid, Spain) and J. Teixidó (Centro de Investigaciones Biológicas, CIB/CSIC, Madrid, Spain), respectively. Jurkat cells were obtained from the American Type Culture Collection (CRL-10915). When needed, CXCR4-AcGFP (20 μg), CD4-YFP (20 μg) or pEYFP-N1 + pcDNA3.1 (1 μg + 19 μg) were nucleofected into Jurkat CD4<sup>+</sup> or Jurkat cells with a BioRad electroporator ( $20 \times 10^6$  cells/400  $\mu$ L RPMI 1640 with 10% FCS). Cells were analyzed 24 h after transfection. Notation of the Jurkat cell types used in the study is summarized in Table S2. Human primary naive CD4+ T lymphocytes (T cells) were isolated from buffy coats by centrifugation through Ficoll-paque plus (GE Healthcare) density gradients (760 xg, 45 min, room temperature (RT)) and negative selection using Dynabeads (Invitrogen Dynal).

#### **Mice**

Murine neutrophils were purified from bone marrow cells of 4- to 6-week-old C57BL/6 mice (Envigo) by centrifugation through Histopaque density gradients (1.077 over 1.119 mg/ml; 940 xg, 30 min, RT, no brake). Mice were handled according to national and European Union guidelines, and experiments were approved by the Comité Ético de Experimentación Animal, Centro Nacional de Biotecnología and the Regional Government (PROEX 250-16).

# **METHOD DETAILS**

#### **Antibodies**

Antibodies used were monoclonal anti-CXCR4 (clone 44717, R&D), -human CXCR4-biotin (12G5, R&D) and -CD4 (OKT-4, eBioscience); polyclonal donkey anti-mouse IgG(H+L)-AF647-conjugated (Jackson Immunoresearch), polyclonal goat anti-mouse IgG(H+L)-AF488 (Invitrogen), anti-Gαi₁ (I-20), -phospho-ERK1,2 (sc-7383; both from Santa Cruz Biotechnology), anti-phospho-Akt (Ser473) and -Akt (#9272; both Cell Signaling Technology). Streptavidin-SPRD was from Beckman Coulter.

#### Reagents

CXCL12, CCL21 and CXCL13 was obtained from PeproTech. Latrunculin A (LatA) and nocodazole were from Sigma-Aldrich. Brefeldin A (ab120299), PitStop2 (ab120687) and PitStop2 negative control (ab120688) were from Abcam. Synthetic peptides, unlabeled or biotinylated, included <sup>192</sup>TMV: NDLWVVV; <sup>221</sup>TMV: IIISKLSH; <sup>239</sup>TMVI: KPTVILILA; <sup>261</sup>TMVI: IDSFILLE and <sup>297</sup>TMVII: LNPILYA and were obtained (≥95% purity) from GenScript (Hong Kong).

#### **Fusion proteins and expression vectors**

The mGluR1α-YFP and 5HT<sub>2B</sub>-YFP plasmids were kindly donated by Dr. Rafael Franco (Universidad Autónoma de Barcelona, Spain). Human CXCR4 receptor was PCR-amplified from pcDNA3.1-CXCR4 using oligonucleotides 5'HindIII (5'ATAAGCTTATGG AGGGGATCAGTATATACATTC3') and 3'Agel (5'GACCGGTG GATCCCGTAAGCTGGAGTGAAAACTTGAAG3') cloned into pECFP-N1, pEYFP-N1, pAcGFPm-N1 (Clontech Laboratories).

Human CD4 was cloned by PCR from T lymphocytes using the oligonucleotides 5'XhoI (5'TTCTCG AGATGAACCGGGG AGTCCCTTTTAG3') and 3'HindIII (5'AAGCTTTAAAATGGGGCTACAT GTCTTCTG3') and cloned into pECFP-N1 and pEYFP-N1.

Human CD86 was cloned by PCR from Raji cells using oligonucleotides 5'Kpnl (5'AAGGTACCAT GGATCCCCAGTGCACTATG3') and 3'Agel (5'ACCGGTTTAAAACATGTATCACTTTT GTGC3') and cloned into pAcGFP-N1.

The  $G\alpha_{i1}$  protein-RLuc construct was obtained as described (Ayoub et al., 2007). Briefly, we inserted an EcoRl site between positions encoding I93 and D94 using pcDNA3.1- $G\alpha_{i1}$  as template (UMR cDNA Resource Center, University of Missouri-Rolla, MO); using the EcoRl site, we then inserted the Renilla luciferase coding region. pcDNA3.1- $G\beta$ 1 and pcDNA3.1- $G\gamma$ 2 were from the cDNA Resource Center (http://www.cdna.org/, Bloomberg, PA).

The CXCR4 mutant (CXCR4mut) was generated by PCR using full-length CXCR4-CFP, CXCR4-YFP or CXCR4-AcGFP as template, the QuickChange Site-Directed Mutagenesis (Stratagene), with the following specific primers: Fw 5' GGCGAAGAAAGCCGC GATGAGGATGGCTGTGGTCTCG AGGGCCTTGCG 3' and Rv 5' CGCAAGGCCCTCGAGACCACAGCCATCCTCATCGCGGCTTT CTTCGCC 3'.

To downregulate endogenous CXCR4 expression, Jurkat and Jurkat CD4<sup>+</sup> cells were electroporated with siRNA CXCR4 specific for the 3′ UTR (1 μM, A-005139-14, Dharmacon; JK<sup>-</sup> and JK<sup>-</sup>CD4, respectively); flow cytometry was used to test for CXCR4 at different times, using specific antibodies.

# **Production of monomeric AcGFP protein**

The AcGFP monomeric protein was cloned using the pAcGFP-N1 vector (Clontech) as template with the primers 5'Ndel (5'AACATATGGTGAGCAGGCGCG3') and 3'BamHI (5'GGATCCGAG CTGCCACGCGGAACCAGCTTGTACAGCTCATCC ATGCC3'), and then cloned into pET-22 (+) (Novagen). We also included a thrombin sequence and 6His before the stop codon. We then transformed BL21 bacteria and confirmed AcGFP protein production. The colony with the highest AcGFP protein levels was cultured in LB medium plus ampicillin (100  $\mu$ g/ml; ON, 37°C with continuous rocking at 200 rpm). In optimal growth conditions, IPTG (0.1 mM) was added to induce protein expression (4 h). The pellet was collected by centrifugation (4,300 xg, 30 min, 4°C) and lysed with 5 mL lysis buffer (50 mM NaH<sub>2</sub>PO<sub>4</sub>, 300 nM NaCl, 2 mM imidazole pH 8.0) plus protease inhibitors. After three freeze-thaw and sonication cycles, extracts were centrifuged (23,000 xg, 30 min, 4°C), the supernatant diluted to 50 mL with lysis buffer, and filtered (0.45  $\mu$ m). AcGFP protein was purified first on a cobalt column (Talon affinity resin, Clontech) followed by a molecular exclusion analytical column (S200). Fractions were analyzed in 12% SDS-PAGE in reducing and non-reducing conditions. Pure monomeric AcGFP was aliquoted and stored at  $-20^{\circ}$ C.

#### **FRET** experiments

# FRET saturation curves by sensitized emission

We transiently transfected 293T or 293CD4 cells (3 × 10<sup>5</sup> cells/well) with cDNA encoding the fusion proteins using the poly-ethylenimine method (Sigma-Aldrich). For CXCR4 homodimers we used a constant amount of CXCR4wt-CFP (2 μg) and increasing amounts of CXCR4wt-YFP (0.25-4.25 μg) (Figures 3A and 6G), or CXCR4mut-CFP (2 μg) and increasing amounts of CXCR4mut-YFP (0.25-4.25 μg) (Figure 6G). As control we used a constant amount of CXCR4-CFP (2 μg) and increasing amounts of mGluR1- $\alpha$ -YFP (0.5-5.5  $\mu$ g; Figure 3A). For CD4/CXCR4 heterodimers, we cotransfected 293T cells (3  $\times$  10<sup>5</sup> cells/well) with a constant amount of CD4-CFP (2 μg) or CXCR4-CFP (1 μg) and increasing amounts of CXCR4-YFP (0.5-4.0 μg) or CD4-YFP (0.25-4.5 μg), respectively (Figures S3A and S3B). As control we used constant amount of CD4-CFP (1 μg) and increasing amounts of 5HT<sub>2B</sub>-YFP (1.0-15.0 μg; Figure S3A). We incubated cells with cDNA and poly-ethylenimine (5.47 mM in nitrogen residues) and 150 mM NaCl in serum-free medium, which was replaced after 4 h by complete medium. At 48 h posttransfection, cells were washed twice in HBSS supplemented with 0.1% glucose and resuspended in the same solution. Total protein concentration was determined for whole cells using a Bradford assay kit (Bio-Rad). Cell suspensions (20 μg protein in 100 μl) were pipetted into black 96-well microplates and emission light was quantified using the Wallac Envision 2104 Multilabel Reader (PerkinElmer) equipped with a high-energy xenon flash lamp (donor: receptor fused to C-CFP, 8 nm bandwidth excitation filter at 405 nm; and the acceptor: receptor fused to -YFP, 10 nm bandwidth excitation filter at 510 nm). Gain settings were identical for all experiments to maintain a constant relative contribution of fluorophores to the detection channels for spectral imaging and linear unmixing. To determine the spectral signature, 293T cells were transiently transfected with the receptor fused to CFP or YFP. The contribution of CFP and YFP alone was measured in each detection channel, and normalized to the sum of the signal obtained for both channels (Zimmermann et al., 2002). The spectral signatures of CFP- or YFP-fused CXCR4wt or mutant, -CD4, -5HT<sub>2B</sub> and -mGluR1α did not vary significantly (p > 0.05) from the signatures determined for each fluorescent protein alone. For FRET quantitation in saturation curves and protein-YFP expression quantitation, the spectral signature was taken into consideration for linear unmixing to separate the two emission spectra.

To determine the fluorescence emitted by each fluorophore in FRET experiments, we applied the following formulas: CFP = S/(1+1/R) and YFP = S/1+R, where S = ChCFP + ChYFP,  $R = (YFP_{530}Q - YFP_{510})/(CFP_{510} - CFP_{530}Q)$  and Q = ChCFP/ChYFP. ChCFP

and ChYFP represent the signal in the 510 nm and 530 nm detection channels (Ch); CFP<sub>510</sub>, CFP<sub>530</sub>, YFP<sub>530</sub> and YFP<sub>510</sub> represent the normalized contributions of CFP and YFP to channels 510-530, as determined from spectral signatures of the fluorescent proteins.

FRET<sub>50</sub> and FRET<sub>max</sub> values were obtained by extrapolating data using a non-linear regression equation applied to a single binding site model with a 95% confidence interval (GraphPad PRISM 5.0). We analyze the FRET<sub>50</sub> and FRET<sub>max</sub> values in those FRET saturation curves that are equal. We generated specific software in MATLAB (The MathWorks, Natick, MA) to analyze whether n FRET saturation curves ( $n \ge 3$ ) are equal (accept H<sub>0</sub>) or are different (reject H<sub>0</sub>) using different statistical tests (F test, Bootstrap and AICc; (Baíllo et al., 2013).

We also used 293T or 293CD4 (9  $\times$  10<sup>6</sup>) cells cotransfected at a fixed CXCR4-YFP/CXCR4-CFP ratio (15 and 9  $\mu$ g, respectively) to evaluate the effect of CD4 co-expression on CXCR4 homodimerization (Figure 3B), and 293T (9  $\times$  10<sup>6</sup>) cells cotransfected at a fixed CXCR4-YFP/CXCR4-CFP ratio (15 and 9  $\mu$ g, respectively) to evaluate the effect of the treatment with LatA (1  $\mu$ M, 15 min, 37°C) or ethanol (control) before CXCL12 activation (100 nM, 15 min, 37°C in continuous rocking; Figure 4A). Where indicated, cells were pretreated with transmembrane peptides (155TMIV and 239TMVI, 50  $\mu$ g/ml, 30 min, 37°C) or DMSO (diluent, control) before CXCL12 activation as above (Figure 6C).

#### FRET by acceptor photobleaching

FRET was measured by photobleaching in 293T cells transiently cotransfected with CXCR4-CFP (0.3 μg)/CD4-YFP (0.75 μg), CXCR4-CFP (0.2 μg)/mGluR1α-YFP (0.8 μg), and CD4-CFP (0.4 μg)/CXCR4-YFP (0.6 μg), CD4-CFP (0.2 μg)/5HT<sub>2B</sub>-YFP (0.8 μg) constructs; concentrations were chosen to assure a YFP:CFP ratio in which receptor pairs reach the maximum FRET efficiency in each case. Cells (3.5 × 10<sup>4</sup> cells/well) were cultured in coverslip chambers (Nunc, Roskilde, Denmark) precoated with fibronectin (10 µg/ml, 60 min, 37°C) and imaged on an Olympus confocal microscope 48 h after cDNA transfection. In a typical FRET experiment, an image of the cell region of interest was taken using standard spectroscopic settings. CFP and YFP were excited with separate sweeps of the 405- and 515-nm lines, respectively, of a laser diode (25 mW at 7%) and a three-line argon laser (45 mW maximum output, 7%-10%), respectively, and directed to the cell via a 405-440/515-nm dual dichroic mirror. Emitted fluorescence was split via a short-pass dichroic mirror 510-nm dichroic mirror for CFP, and directed to a spectral detector adjusted to a 460- to 500-nm range. For YFP, fluorescence was directed to a spectral detector adjusted to a 530- to 570-nm range. Confocal fluorescence intensity data (ICFPpre, IYFPpre) were recorded, with a pinhole of 100, as the average of four line scans per pixel and digitized at 12 bits. Repeated scans with 515 nm maximum light intensity were used to photobleach YFP, which required 5 s at maximal scan rates and maximum pinhole aperture. After YFP bleaching, fluorescence intensity (ICFPpost, IYFP- post) was measured using identical parameters. FRET efficiency was determined on a pixel-by-pixel basis (E) and calculated in percentage as E = [(ICFPpost -ICFPpre)/ICFPpost] x 100, where ICFPpre and ICFPpost are the background-corrected CFP fluorescence intensities before and after YFP photobleaching, respectively, using ImageJ 1.40 g software (National Institutes of Health). As a negative control, FRET was determined in 293T cells transiently transfected with CXCR4-CFP or CD4-CFP alone (this FRET efficiency was substracted at each FRET efficiency value analyzed by the heterodimer CXCR4/CD4 and CD4/CXCR4, respectively). We also analyzed FRET efficiency for controls, CXCR4-CFP/mGluR1α-YFP or CD4-CFP/5HT<sub>2B</sub>-YFP (Figure S3D). FRET efficiency was calculated from ≥ 20 images for each of three independent-experiments.

# **BRET**

293T (6 × 10<sup>5</sup>) cells were transiently cotransfected with a constant amount of cDNA encoding  $G\alpha_{i1}$ -Rluc (0.5 μg), pcDNA3.1-Gβ<sub>1</sub> + pcDNA3.1-Gγ<sub>2</sub> (0.5 μg, 1:1 ratio) and increasing amounts of cDNA for X4wt-YFP or X4mut-YFP (0.15 - 3.5 μg). As control of interaction specificity we transiently cotransfected 293T cells with constant amount of  $G\alpha_{i1}$ -Rluc (0.5 μg), pcDNA3.1-Gβ<sub>1</sub> + pcDNA3.1-Gγ<sub>2</sub> (0.5 μg, 1:1 ratio) and increasing amounts of 5HT<sub>2B</sub>-YFP (0.15 - 8.0 μg). The 5HT<sub>2B</sub> receptor is a GPCR coupled to  $Gq_{11}$  protein (McCorvy and Roth, 2015). Fluorescent proteins were quantified using the Wallac Envision 2104 Multilabel Reader (PerkinElmer) equipped with a high-energy xenon flash lamp (10 nm bandwidth excitation filter at 510 nm) as described, using coelenterazine H (5 μΜ, 1 min, RT) (Martínez-Muñoz et al., 2014).  $G\alpha_{i1}$ -Rluc luminescence signals were acquired 10 min after coelenterazine H addition. BRET efficiency (BRET<sub>eff</sub>) is defined as [(long wavelength emission)/ (short wavelength emission)]-Cf, where Cf is [(long wavelength emission)/(short wavelength emission)] for the Rluc construct expressed alone in the same experiment. BRET signal is expressed as mili-BRET units (mBU). In each BRET titration curve, the relative amount of acceptor is given by the ratio between acceptor fluorescence (YFP) and donor luciferase activity (Rluc) (Figures S5C–S5F).

For BRET at a fixed ratio, 293T or 293CD4 cells (9  $\times$  10<sup>6</sup>) were cotransfected with G $\alpha_{i1}$ -Rluc (3  $\mu$ g), pcDNA3.1-G $\beta_1$  + pcDNA3.1-G $\beta_2$  (3.0  $\mu$ g, 1:1 ratio) and X4wt-YFP or X4mut-YFP (15  $\mu$ g). At 48 h post-transfection, cells were detached with HBSS + 0.1% glucose (37°C) and distributed in a 96-well microplate (0.3  $\mu$ g/ $\mu$ l, 90  $\mu$ l). Coelenterazine H was added (5  $\mu$ M final concentration, 100  $\mu$ l/well) and readings started by adding CXCL12 to the cells (determinations were obtained at 0.05 s intervals until 0.5 s) using the Wallac Envision 2104 Multilabel Reader equipped with an automatic injector. When needed, cells were pretreated with LatA (1  $\mu$ M, 15 min, 37°C) before CXCL12 stimulation (100 nM). BRET signal was expressed in BRET units (BU) at the ratio described above.

# Sample preparation for STED imaging

Jurkat CD4<sup>+</sup> cells and human naive CD4<sup>+</sup> T lymphocytes (T cells) ( $7.5 \times 10^4$ /well) were plated on slides (1.5H; MatTek) coated with fibronectin ( $10 \mu g/ml$ , 1 h,  $37^{\circ}C$ ), then stimulated with CXCL12 (100 nM, 5 min,  $37^{\circ}C$ ,  $5\% CO_2$ ). Cells were fixed with 4% PFA (10 min, RT) and non-specific binding was blocked with PBS containing 1% BSA, 0.1% goat serum and 50 mM NaCl (30 min,  $37^{\circ}C$ ). Cells

were stained with anti-CXCR4 mAb (clone 44717,  $10 \,\mu\text{g/ml}$  to ensure saturating conditions,  $30 \,\text{min}$ , RT), followed by AF488-goat anti-mouse IgG(H+L) ( $10 \,\mu\text{g/ml}$  to ensure saturation conditions,  $30 \,\text{min}$ , RT). Slides were mounted with Prolong Antifade medium (ThermoFisher). As control, we confirmed anti-CXCR4 mAb (clone 44717) specificity on Jurkat CD4<sup>+</sup> KO cells by STED (stimulated emission depletion) and detected no fluorescence (not shown).

#### **STED** imaging

STED super-resolution images of Jurkat CD4 $^{+}$  and T cells were acquired with a confocal microscope (Leica TCS SP8, Leica Microsystems) equipped with an oil immersion objective (HCX PL APO CS x100, Leica) with a 1.4 numerical aperture. Samples were excited with a WLL2 laser at 47.9% power (2.2  $\mu$ W), and fluorescence detected in the 498-560 nm range. STED laser beam intensity (592 nm) was set to 100% of its power (14 mW); images (1024 × 1024 pixels, 18.94 nm per pixel) were acquired with a line average 2, a frame accumulation of 8, and a scanning speed of 200 Hz. In these conditions, no significant fluorescence photobleaching was observed.

#### **STED** image analysis

Super-resolution images were analyzed using custom software written in MATLAB that allows automatic detection of fluorescent spots and their fit to a point spread function (PSF) profile, thus providing intensity and centroid position of each spot. Details of the image analysis procedure were as follows. First, the PSF profile and its full-width-at-half-maximum (FWHM) were determined based on calculation of autocorrelation of STED images for fluorescent markers (the same labeled antibodies used for cell imaging) sparsely absorbed on glass coverslips (Veatch et al., 2012). In these sparse conditions, we guaranteed that we were observing individual labeled antibodies and thus the FWHM of individual spots on glass reflects the effective STED resolution. In our experimental conditions the optical resolution resulted  $\sim$ 60 nm. The autocorrelation curves were fitted according to a Gaussian and a Lorentz PSF profile, as expected for STED imaging. The model providing the best fit based on  $\chi^2$  calculation and the corresponding FWHM were used for further analysis. STED images on cells were analyzed by a previously reported algorithm to detect the coordinates of the centroid positions of local maxima corresponding to bright fluorescence spots. The centroid positions of the spots were convoluted with the PSF kernel, and a least-squares fitting routine was used to determine the intensity of each spot.

To estimate the stoichiometry of the fluorescence spots we compared results of the fitting analysis of sparse fluorescent spots from non-specific antibody binding to glass coverslips to that of markers labeling receptors on cell membranes, obtained under identical experimental conditions (Torreno-Pina et al., 2016; van Zanten et al., 2009). Compared to spots on glass, intensity histograms for spots retrieved on cells generally showed broader distribution and greater intensity, indicative of receptor nanoclustering. To use the intensities I to estimate the number of receptors in the spots, we fitted their histogram to a model distribution  $g_N(I)$  composed of a linear combination of functions

$$g_N(I) = \sum_{n=1}^N \alpha_n \cdot f_n(I),$$

where  $f_n$  represents the distribution intensity for a spot containing n receptors,  $\alpha_n$  is the relative weight of this distribution so that  $\sum_{n=1}^{N} \alpha_n = 1$ , and N is the maximum number of receptors (Moertelmaier et al., 2005). We considered that the distribution of intensity for a spot containing n receptors could be obtained recursively as

$$f_n = f_{n-1} \otimes f_1$$

where  $\otimes$  represents the convolution (Moertelmaier et al., 2005; Schmidt et al., 1996; Torreno-Pina et al., 2016; Zanacchi et al., 2017). To model our data, we used a lognormal distribution for  $f_1$ :

$$f_1(I) = \frac{1}{\sqrt{2\pi}\sigma I} e^{-\frac{(\ln I - \mu)^2}{2\sigma^2}}$$

as it provided the best data fit among several distributions tested. In addition, the lognormal distribution is a close approximation of the expected theoretical distribution for the intensity corresponding to the detection of a fluorescent emitter (Moertelmaier et al., 2005; Schmidt et al., 1996; Zanacchi et al., 2017). The intensity value is given by the product of an exponential distribution (representing the expected probability for the intensity) with a sigmoid response function (describing the limited detection rate for emitters with low intensity and/or signal-to-noise ratio). The distribution of intensity detected for spots on glass was used as a calibration standard to estimate the parameters  $\mu$  (mean) and  $\sigma$  (standard deviation) of the lognormal distribution, through its fit to a linear combination of N = 2 functions. These parameters were used to fit the intensity distribution of spots in cell membranes, from which values for  $\alpha_n$  were obtained.

# Sample preparation for SPT

Jurkat or Jurkat CD4<sup>+</sup> cells were electroporated with CXCR4-AcGFP (JK or JKCD4, respectively). SPT (single-particle tracking) experiments require low expressing conditions in order to follow individual trajectories (Manzo and Garcia-Parajo, 2015). Thus, at 24 h post-transfection, cells expressing low CXCR4-AcGFP<sup>+</sup> levels were selected by sorting in a MoFlo Astrios Cell Sorter

(Beckman-Coulter). Using a Dako Qifikit; (DakoCytomation), we quantified the number of CXCR4 receptors and found ~8,500 -22,000 CXCR4-AcGFP receptors/cell, that correspond to a particle density  $\sim$ 2 - 4.5 particles/ $\mu$ m<sup>2</sup>. These cells were resuspended in RPMI supplemented with 2% FBS, NaPyr and L-glutamine and plated on p96 well plates for at least 2 h in culture. Cells were centrifuged and resuspended in a buffer with HBSS, 25 mM HEPES, 2% FBS (pH 7.3) and plated on glass-bottomed microwell dishes (MatTek Corp.) coated with fibronectin (Sigma-Aldrich, 20 μg/ml, 1 h, 37°C). To observe the effect of the ligand, we coated dishes with CXCL12 (100 nM, 1 h, 37°C); cells were incubated (20 min, 37°C, 5% CO<sub>2</sub>) before image acquisition.

The study the effect of the actin cytoskeleton, cells were pretreated with LatA (1 μM, 15 min, 37°C). To exclude the possibility of observing vesicle transport we used nocodazole (1 µg/ml, 15 min, 37°C) to disrupt microtubules, or treated the cells with brefeldin A (10 μg/ml, 30 min, 37°C) to block intracellular protein transport. Ethanol, DMSO or PBS were the diluents for LatA, nocodazole and brefeldin, respectively. As cell membrane fluidity could be affected by these diluents (Gurtovenko and Anwar, 2007; Patra et al., 2006), we included them as controls.

To study the effect of the antagonist CXCR4 peptide, JKCD4 cells were pre-treated with <sup>221</sup>TMV (control peptide) or with <sup>239</sup>TMVI (125 μg/ml, 30 min, 37°C, 5%CO2). As an additional control, JKCD4 cells were also pre-treated with DMSO (peptide diluent).

Jurkat CD4<sup>+</sup> cells were electroporated with siRNA CXCR4 specific for the 3' UTR (1 μM A-005139-14, JK) or with non-targeting siRNA (1 μM, siControl; B-001810-10, both from Dharmacon; JK°). CXCR4 expression at the membrane was analyzed by flow cytometry at 24 h post-transfection. When endogenous CXCR4 had been downregulated (> 85%-90%), JK<sup>-</sup> cells were electroporated with CXCR4wt-AcGFP (JKCD4 wt) or with CXCR4mut-AcGFP (JKCD4 mut) and JKCD4 with CXCR4mut-AcGFP (JKCD4 mut) and sorted 24 h later, as described.

When needed, cells were pre-treated with PitStop2, with PitStop2 negative control (10 min, 37°C, 5% CO<sub>2</sub>) or with DMSO as a solvent control and placed on coated dishes. As we studied CXCL12-mediated clustering and not its lateral diffusion, cells were fixed (PFA 4%, 20 min, RT) prior to TIRF analysis.

#### Single-particle tracking (SPT) measurement

Experiments were performed using a total internal reflection fluorescence (TIRF) microscope (Leica AM TIRF inverted) equipped with an EM-CCD camera (Andor DU 885-CS0-#10-VP), a 100x oil-immersion objective (HCX PL APO 100x/1.46 NA) and a 488-nm diode laser. The microscope was equipped with incubator and temperature control units; experiments were performed at 37°C with 5% CO<sub>2</sub>. To minimize photobleaching effects before image acquisition, cells were located and focused using the bright field, and a fine focus adjustment in TIRF mode was made at 5% laser power, an intensity insufficient for single-particle detection that ensures negligible photobleaching. Image sequences of individual particles (500 frames) were acquired at 49% laser power with a frame rate of 10 Hz (100 ms/frame). The penetration depth of the evanescent field used was 90 nm.

#### Single particle tracking analysis

Particles were detected and tracked using previously described algorithms (U-Track2; (Jaqaman et al., 2008)) implemented in MATLAB. Briefly, particle subpixel positions and intensities were calculated by detecting significant local intensity maxima that depends on image contrast and noise in the images. The algorithm fitted a Gaussian mixture model to simultaneously fit for particles with overlapping signals, enhancing detection accuracy and resolution. Particles were tracked using a two-step particle tracking algorithm to generate complete trajectories by closing gaps and by capturing merging and splitting events. First, the algorithm linked particles between consecutive frames to generate tracks that started and ended, due to true particles that appear and disappear as well as particles that disappear temporarily due to merging and splitting. The algorithm then generated complete particle trajectories by linking the track segment in three ways: end-to-start, to close gaps resulting from temporary particle disappearance; end-to-middle, to capture particle merging events; and middle-to-start, to capture particle splitting events. For each step and each particle, a cost is assigned to every potential event (e.g., particle blinking, merging, splitting, appearing, or disappearing) and the solution that minimizes the sum of the costs is selected. This allowed us to track a particle beyond a blinking event. Only tracks longer than 20 frames were used for further analysis; particles that merged or splitted and those located out of the cell body (filopodia) were excluded. Short tracks caused by noise from blinking events were discarded. All movies were analyzed using the same tracking parameters. To further ensure faithful reconstruction of each trajectory, we implemented a separate window that allowed for visual supervision. Individual trajectories were used to generate meansquare-displacement (MSD) plots. The MSD of each trajectory was calculated according to the following equation (Simson et al., 1995):

$$MSD(n.\Delta t) = \frac{1}{N-n-1} \sum_{j=1}^{N-n-1} \left[ x(j\Delta t + n\Delta t) - x(j\Delta t) \right]^2 + \left[ y(j\Delta t + n\Delta t) - y(j\Delta t) \right]^2$$

where  $\Delta t$  is the time increment, N is the total number of frames of the trajectory, n the time lag index, and  $[x(j\Delta t + n\Delta t) - x(j\Delta t)]$  and  $[y(j\Delta t + n\Delta t) - y(j\Delta t)]$ , particle displacement after time  $t = n\Delta t$  along the x and y axes, respectively. Short-time lag diffusion coefficients were extracted from a linear fit to the first through fourth point of the MSD curve using the following equation:

$$MSD = 4D_{1-4}t + \Delta_0$$

where  $D_{1-4}$  is the short-time lag diffusion coefficient and  $\Delta_0$  is the MSD offset at zero timelag. Distribution of  $D_{1-4}$ , from which median diffusion coefficients were calculated, typically resulted from the analysis of thousands of single trajectories over multiple cells (statistics provided in the respective figure captions).

#### Minimum detectable diffusion coefficient

To determine the minimum detectable diffusion coefficient in our experimental conditions, we used both, purified AcGFP monomeric proteins immobilized on glass coverslips and fixed Jurkat CD4 $^+$  cells electroporated with CXCR4-AcGFP (JKCD4). Cells were seeded onto glass coverslips (30 min) and fixed with 4% PFA (20 min). As 95% of the immobile AcGFP monomeric protein or fixed JKCD4 cells showed a diffusion coefficient  $\leq 0.0015 \ \mu m^2.s^{-1}$ , this value was set as the threshold to discriminate between immobile and mobile trajectories.

#### **Trajectory analysis**

The MSD plots shown in Figure 1E were fitted according to a general anomalous diffusion model represented by the power law (Manzo and Garcia-Parajo, 2015):

$$MSD = MSD_0 + 4Dt^{\alpha}$$

where  $\alpha$  is the anomalous exponent and  $MSD_0$ , a constant offset. The value of the exponent  $\alpha$  was used to determine whether particle motion was considered confined  $(0 < \alpha < 0.6)$ , Brownian  $(0.9 < \alpha < 1.1)$ , or directed  $(\alpha > 1.1)$ . Moreover, in the case of confined motion, we determined the confinement size L, using the relation (Destainville and Salomé, 2006):

$$L = \sqrt{3(\langle r^2 \rangle + MSD_0)}$$

To classify the type of motion exhibited by individual trajectories, we used the moment scaling spectrum (MSS) (Ewers et al., 2005). According to this analysis, trajectories longer than 50 frames could be classified as confined, Brownian or directed, depending on the value of their first moment. For each experimental trajectory, we generated a distribution of moments based on 500 simulated trajectories with Brownian motion, having the same diffusion coefficient and length as the trajectory analyzed. Trajectories with a first moment between 2.5% and 97.5% of the distribution obtained from simulations were considered Brownian. In contrast, trajectories whose first moment value was below 2.5% (above 97.5%) of the distribution obtained from simulations were classified as confined (directed).

#### **Particle stoichiometry determination**

To determine the number of receptors per particle from the intensity information contained in the SPT trajectories, we developed additional MATLAB routines. For each particle detected, we measured the intensity of pixels around the particle (in a 3x3 pixel matrix whose central position is given by the coordinates x,y obtained by U-Track2), in each frame along its trajectory. We also estimated the particle background ( $K_0$ ) for each frame.  $K_0$  for each frame was calculated by locating the cell in the video and analyzing the intensities of the cell background in each frame.  $K_0$  was chosen as the gray value at a given quantile of this distribution (80%). The intensity value for each particle is then given by the difference between particle intensity and the background in each frame. To minimize photon fluctuations within a given frame, we as particle intensity the average value (background subtracted) obtained over the first 20 frames. To ensure that within this range of frames we did not have photobleaching events that would affect the quantitation of the data, we measured the photobleaching times (s) from individual CD86-AcGFP (electroporated on Jurkat CD4<sup>+</sup> cells, (Dorsch et al., 2009)) particles that exclusively showed a single photobleaching step. Fitting of the distribution to a single exponential decay renders a  $\tau_0$  value of  $\sim$ 5 s, which corresponds to 50 frames (100 ms/frame).

The total number of receptors/particles was finally estimated by dividing the average particle intensity by the particle intensity arising from individual AcGFP molecules. To unequivocally identify the intensity emitted by an individual AcGFP, we used as calibration Jurkat CD4 $^+$  cells electroporated with the monomeric CD86-AcGFP. We performed SPT experiments on CD86-AcGFP and analyzed the data in similar way as described above. Distribution of monomeric particle intensities was analyzed by Gaussian fitting rendering a mean value of 1336  $\pm$  156 a.u. This value was then used as the monomer reference to estimate CXCR4-AcGFP particle size (see Figures S1D–S1F).

As we were interested in comparative analysis of distinct experimental conditions, TIRF data are shown as cumulative data. In such conditions, we cannot include SD values for most of the determinations. All TIRF experiments were repeated independently at least three times, with a minimum of 8-25 cells in each experiment. Statistics for each experimental condition are provided in the corresponding figure captions.

# **Modeling of oligomeric CXCR4**

We used the crystal structures for CXCR4 published by Wu and collaborators (Wu et al., 2010) to select peptide candidates. We used the coordinates for the crystal structures described (PDB codes: 30DU, 30E0, 30E8, 30E9, 30E6) as templates to evaluate potential surfaces involved in CXCR4 oligomer formation. These coordinates were loaded into PyMOL molecular graphics software and symmetry-related molecules were generated to study crystal packing in the structure. To search for transmembrane (TM) helix

segments potentially involved in lateral interactions between receptors, we analyzed potential dimer contacts with adjacent dimers, selected, and synthesized fragments for TM domains IV, V, VI and VII to study their effect on receptor oligomerization. Of the initial 20 peptides obtained, some were insoluble and discarded; the remainder were screened in a chemotaxis assay for their ability to block CXCL12-mediated responses.

#### Flow cytometry analysis

Cells were plated in V-bottom 96-well plates (2.5 × 10<sup>5</sup> cells/well) and incubated with specific antibodies (30 min, 4°C), followed by second antibodies where needed. Cell-bound fluorescence was determined in a Gallios flow cytometer (Beckman Coulter).

To test CXCR4wt or CXCR4mut expression, we used Jurkat CD4<sup>+</sup> cells with endogenous CXCR4 downregulated using specific siRNA (Jurkat CD4). These cells were electroporated with the CXCR4wt-AcGFP (JK CD4 wt) or with CXCR4mut-AcGFP (JK CD4 mut). CXCR4 expression was analyzed 24 hours post-transfection, using anti-CXCR4 (clone 44717) and donkey anti-mouse IgG (H+L) Alexa Fluor 647 (Figure S6C).

Receptor internalization was determined by flow cytometry on JKCD4 wt and JKCD4 mut cells activated at indicated times with CXCL12 (20 nM). Results are expressed as a percentage of the mean fluorescence intensity of treated cells relative to that of unstimulated cells (Figure S6D).

#### **Calcium determination**

Jurkat cells electroporated with CD4-CFP or CFP, Jurkat CD4<sup>+</sup> cells pre-treated with ethanol (control) or LatA (1 μM, 15 min, 37°C), KG1a cells (2 × 10<sup>6</sup> cells/ml) transfected with CXCR4wt-CFP or CXCR4mut-CFP, and primary naive CD4<sup>+</sup> T lymphocytes were resuspended in RPMI with 10% FCS and incubated with Fluo-3AM (Invitrogen, Molecular Probes; 0.28  $\mu$ g/ $\mu$ l in DMSO, 16  $\mu$ l/10 cells; 30 min, 37°C). Cells were washed, resuspended in RPMI with 2 mM CaCl<sub>2</sub>, and maintained at 4°C until activation. Ca<sup>2+</sup> flux in response to different concentrations of CXCL12 (10-50 nM, 37°C) was measured at 525 nm in an EPICS XL flow cytometer (Beckman Coulter). Data, analyzed using FlowJo 8.2 (Intel), are expressed as a percentage of the maximum signal (100%).

## **Transwell migration assay**

Cells (3 × 10<sup>5</sup> cells in 0.1 ml) were placed in the upper well of uncoated 24-well transmigration chambers (3 µm pore; Transwell, Costar, Cambridge, MA). CXCL12 (20 nM) in 0.6 mL RPMI with 0.1% BSA and 10 mM HEPES were added to the lower well. Plates were incubated (180 min, 37°C, 5% CO<sub>2</sub>) and cells that migrated to the lower chamber were counted by flow cytometry, corrected for variations in input concentration and expressed as a percentage of cell migration. To determine the effect of CD4 co-expression, Jurkat cells were electroporated with CD4-YPF or with the empty vector YFP and 24 h post-transfection migration was assessed as above. To evaluate the specificity of TM-peptide treatment, KG1a cells were electroporated with CXCR4-YFP, with CXCR5-YFP, or with CCR7-YFP. At 24 h post-transfection, cells were pretreated (30 min, 37°C, 5% CO<sub>2</sub>) with DMSO (control), <sup>221</sup>TMV or  $^{239}$ TMVI peptides (50  $\mu$ g/ml), and placed in the upper well of uncoated 24-well transmigration chambers as above. As chemoattractants, we used CXCL12 (20 nM), CXCL13 (100 nM) or CCL21 (100 nM), as appropriate. When needed, neutrophils purified from bone marrow cells of C57/BL6 mice were pre-treated with DMSO (control), <sup>221</sup>TMV or <sup>239</sup>TMVI peptides (125 μg/ml) or pertussis toxin (PTx; 0.2 μg/ml, 1 h, 37°C, 5% CO<sub>2</sub>) before assessment in cell migration assays.

## Cell adhesion on planar lipid bilayers

Planar lipid bilayers were prepared as described (Carrasco et al., 2004). Briefly, unlabeled GPI-linked ICAM-1 liposomes were mixed with 1,2-dioleoyl-PC. Membranes were assembled in FCS2 chambers (Bioptechs), blocked with PBS with 2% FCS (1 h, RT) and coated with CXCL12 (200 nM, 30 min, RT). Cells (3 × 10<sup>6</sup>cells/ml) in PBS containing 0.5% FCS, 0.5 g/L D-glucose, 2 mM MgCl<sub>2</sub>, and 0.5 mM CaCl<sub>2</sub> were injected into the pre-warmed chamber (37°C) and confocal fluorescence, differential interference contrast (DIC), and interference reflection microscopy (IRM) images were acquired in a Zeiss Axiovert LSM 510-META inverted microscope with a 40x oil-immersion objective. Images were analyzed using Imaris 6.0 software (Bitplane) and ImageJ 1.49v.

#### Western blot and co-immunoprecipitation

CXCR4wt-AcGFP- or CXCR4mut-AcGFP-electroporated KG1a cells (20 × 10<sup>6</sup>) were activated with CXCL12 (20 nM) at indicated times. Cells were lysed in detergent buffer (20 mM triethanolamine, 1% digitionin, 1 mM PMSF, 10 μg/ml aprotinin, 10 μg/ml leupeptin, 10 µM sodium orthovanadate; 30 min, 4°C). Cell extracts immunoprecipitated with anti-GFP mAb (JL-8, Clontech) followed by anti-mouse IgG agarose protein and analyzed by western blot using specific antibodies (Gα; pERK1,2; pAkt; Akt). Densitometry analyses were performed using ImageJ 1.49v and expressed as x-fold increase versus unstimulated cells.

# Biacore kinetics to measure K<sub>D</sub>

For CXCL12 binding analysis, we prepared and characterized lentiviral particles (LVP) bearing CXCR4wt or CXCR4mut as described (Vega et al., 2011). Surface plasmon resonance (SPR) experiments were performed on a Biacore 3000 (GE Healthcare, Pittsburgh, PA, USA). Flow cells of a CM5 sensorchip were functionalized with 8000-8500 resonance units of LVP (Vega et al., 2011). CXCL12 (12.5–200 nM) diluted in HBS buffer (100 μM HEPES, 150 mM NaCl, 0.005% polyoxyethylene sorbitan P20, pH 7.4) were injected over immobilized LVP (30 µl/min, 2 min, 25°C; association phase), followed by a 4-min injection period of HBS buffer alone over the surface (dissociation phase). Sensorgrams were corrected for signals obtained in reference flow channels (sensorchips with immobilized LVP obtained from CXCR4-negative 293T cells or no LVP). For regeneration, sensorchips were washed with 5 mM HCl. All steps were performed using system robotics. Sensorgrams, recorded in real time and expressed in relative units, were used to calculate (simple 1-site interaction model with Biaevaluation 4.1 software; Biacore) kinetic parameters (K<sub>D</sub>, affinity constant).

#### **Adoptive transfer experiments**

For assays to measure *in vivo* neutrophil clearance to bone marrow, neutrophils from donor C57BL/6 mice (4-6 weeks) were isolated as above and labeled with CellTracker Green (CMFDA, 0.1  $\mu$ M, 30 min, 37°C, 5% CO<sub>2</sub>), and pre-treated (2 × 10<sup>6</sup> cells/ml) with DMSO (control), <sup>221</sup>TMV or <sup>239</sup>TMVI peptides (125  $\mu$ g/ml), or PTx (0.2  $\mu$ g/ml; 1 h, 37°C, 5% CO<sub>2</sub>). Neutrophils were resuspended in PBS (10 × 10<sup>6</sup> cells/ml) and injected i.v. (200  $\mu$ l/mouse) into the lateral tail vein. After 1 h, bone marrow cells from recipient mice were harvested. Single cell suspensions were analyzed and CMFDA-positive cells quantified by flow cytometry. Results were expressed as a percentage of the maximum recovered CMFDA-labeled cells (untreated neutrophils).

#### **QUANTIFICATION AND STATISTICAL ANALYSIS**

All results were analyzed using GraphPad PRISM 5.0 (ns,  $p \ge 0.05$ , \*p  $\le 0.05$ , \*\*p  $\le 0.001$ ; \*\*\*p  $\le 0.0001$ ). A two-tailed Mann-Whitney nonparametric test was used to analyze diffusion coefficient (D<sub>1-4</sub>) of single particles (Figure 2A), Ca<sup>2+</sup> flux data (Figures 5A, 5B, and 7C), BRET ratio (Figures 5C and 7B) and FRET efficiency (Figure 7C) data, cell migration assays (Figures 5D, 6B, and 7E) and the percentage of the cell adhesion on lipid bilayers (Figure 7G).

We used contingency tables to compare two or more groups of categorical variables, such as percentages of mobile or immobile particles and particles with different types of motion (confined, brownian/free or direct transport), and were compared using a Chisquare test with a two-tail P value (Figures 2B, 3F, 3H, 4D, 4E, S4E, and S6C).

Comparison of diffusion coefficients ( $D_{1-4}$ ) of single particles in various conditions (Figures 2F, 3E, 3I, 4C, 4F, 6J, S2B, S2D–S2F, S3H–S3J, and S4D), intensity distribution of CXCR4 single trajectories in peptides pre-treated JKCD4 cells (Figure 6D), lipid bilayer data (Figures 5F, 5G, and 5I–5J), the migration of mouse neutrophils (Figure 7H) and the adoptively transferred neutrophils experiments (Figure 7I) were analyzed to determine significant differences between means using one-way ANOVA followed by Tukey's multiple comparison test.